Constraints on Southern Ocean Shortwave Cloud Feedback from the Hydrological Cycle

Chuyan Tan[1], Daniel T. McCoy[1], Gregory S. Elsaesser[2,3]

[1]University of Wyoming
[2]Columbia University, Dept. of Appl. Physics and Appl. Mathematics
[3]NASA Goddard Institute for Space Studies (GISS)

Key Points:

- Enhanced moisture convergence contributes to a negative cloud feedback in the Southern Ocean.
- Southern Ocean liquid water path increased over the past two decades due to enhanced moisture convergence.
- Across global climate models, the sensitivity of upwelling shortwave to cloud opposes the sensitivity of cloud to moisture convergence.

Corresponding author: D. T. McCoy, daniel.mccoy@uwyo.edu

Abstract

Shifts in Southern Ocean (SO, $40{-}85^oS$) shortwave (SW) cloud feedback (SW_{FB}) towards more positive values are the dominant contributor to higher effective climate sensitivity (ECS) in Coupled Model Intercomparison Project phase 6 (CMIP6) models. The positive shift in SW_{FB} in CMIP6 global climate model (GCMs) can be traced back to the greater reduction in low cloud cover and the weaker cloud liquid water response to warming in the SO. To evaluate how realistic the CMIP6 cloud response is, we connect the SO SW_{FB} to changes in column-integrated liquid water mass (LWP) and the susceptibility of albedo to LWP in 50 CMIP5 and CMIP6 GCMs. In turn, we predict the responses of SO LWP to warming using a cloud-controlling factor (CCF) model. The combination of the CCF model and radiative susceptibility explains about 50 % of the variance in the GCM-simulated SW_{FB} in the SO. Observations of SW radiation fluxes, LWP, and reanalysis of CCFs are used to constrain the SO SW_{FB}. This yields a constrained response of SO LWP to warming of $2.89\ -\ 4.41\ g\ m^{-2}\ K^{-1}$, relative to the total GCM range of $-0.48\ -\ 9.33\ g\ m^{-2}\ K^{-1}$. The susceptibility of albedo to LWP is constrained to be $0.41 - 0.86\ (kg\ m^{-2})^{-1}$, relative to the GCM range of $0.23 - 3.62$ $(kg\ m^{-2})^{-1}$, where albedo is unitless. The overall constraint on the contribution of SO SW_{FB} to global cloud feedback is $-0.19\ -\ 0.05\ Wm^{-2}K^{-1}$, relative to GCM range of $-0.28\ -\ 0.27\ Wm^{-2}K^{-1}$. In summary, observations suggest a moderate negative to weak positive SO SW_{FB}.

Plain Language Summary

Clouds over the Southern Ocean (SO, $40{-}85^oS$) efficiently reflect sunlight back to space and cool the planet. Previous studies suggest that SO clouds become optically thicker and thus more strongly cool the planet in response to global warming—a compensating feedback (i.e., a negative shortwave cloud feedback (SW_{FB})). The SO SW_{FB} in the latest generation of global climate models (GCMs) participating in the Coupled Model Intercomparison Project phase 6 (CMIP6) has shifted towards more positive values, leading to the larger predicted temperature responses to greenhouse gas increases by these GCMs. In this study, we examine if this more positive SW_{FB} is consistent with observations. We connect the effect of SO clouds on reflected sunlight to the predicted response of cloud liquid content to global warming. Satellite observations of reflected sunlight, cloud liquid, and reanalysis of atmospheric state are applied to constrain the SO SW_{FB}. The results suggest that SO cloud liquid will increase with warming around the average of GCM predictions. Satellite records suggest that the sensitivity of reflected sunlight to cloud liquid is weak compared to GCMs. In combination, these two constraints suggest a moderately negative SO SW_{FB}.

1 Introduction

Shortwave cloud feedback (SW_{FB}) is the largest uncertainty in net climate feedback, and by extension, effective climate sensitivity (ECS) (Zelinka et al., 2020; Sherwood et al., 2020). This uncertainty can be attributed to the difficulties in representing subgrid-scale cloud processes in the global climate models (GCMs) (Sherwood et al., 2014; Zhao, 2014; Storelvmo et al., 2015; Webb et al., 2015; McCoy et al., 2016). Although there is a large intermodel spread in the sign and magnitude of SW_{FB}, some robust features emerged from previous generations of GCMs. For example, positive SW_{FB} in subtropics due to decreased cloud coverage and negative SW_{FB} in extratropics due to increased cloud optical depth (Zelinka et al., 2012; Ceppi, McCoy, & Hartmann, 2016).

Zelinka et al. (2020) shows that GCMs participating in the Coupled Model Intercomparison Project phase 6 (CMIP6) report positive shifts in extratropical SW_{FB} poleward of 30^o relative to previous generations of GCMs. This results in an increase in ECS in CMIP6 GCMs. Zelinka et al. (2020) demonstrates the positive shift in extratropical SW_{FB} is driven by the stronger reduction of low cloud cover and weaker increase of in-cloud liquid water content in extratropics in response to warming in CMIP6 GCMs. This corresponds to a more positive cloud amount feedback and less negative cloud optical depth feedback, respectively. In this study, observations are used to constrain extratropical SW_{FB} and evaluate whether the more positive SW_{FB} in the Southern Ocean region (SO, defined as $40{-}85^oS$) in CMIP6 GCMs are consistent with observed variability.

Examining the response of cloud liquid water content to warming is an idealized way to constrain extratropical SW_{FB}. The column-integrated liquid water mass (i.e., Liquid Water Path, hereafter LWP) is proportional to the cloud optical depth in an overcast region. Increased in-cloud LWP increases the amount of reflected shortwave (SW) radiation more than it reduces the outgoing longwave (LW) radiation, leading to a negative cloud optical depth feedback (Paltridge, 1980). In this study, LWP is defined as the liquid water mass averaged over cloudy and clear-sky pixels. It incorporates information about cloud fraction (CF) coverage into this variable as well as in-cloud LWP ($LWP \approx CF \cdot LWP_{in-cloud}$).

Across GCMs, SO LWP increases in response to increased surface temperature. Fig 1a shows that the changes in LWP scaled by changes in global-mean surface air temperature (GMT) in the quadrupling CO_2 ($abrupt4xCO_2$) simulations of GCMs are anti-correlated with model extratropical SW_{FB}. The response of LWP to warming also reproduces the dipole pattern of SW_{FB} in the SO. Our analysis will focus on constraining SO SW_{FB} by constraining the changes in LWP with warming in $40 - 85^oS$.

Many potential mechanisms can explain the increase of extratropical LWP with warming, as shown by Fig 1b (Terai et al., 2019). For example, the phase changes of susceptible ice to liquid in the mixed-phased cloud region and the resultant suppression of precipitation (Senior & Mitchell, 1993; McCoy et al., 2014a; Ceppi, Hartmann, & Webb, 2016; Tan et al., 2016, 2019); the strongly increased moist adiabat at high latitudes (Betts & Harshvardhan, 1987); and increases in cloud liquid water content driven by enhanced extratropical moisture convergence (McCoy, Field, Bodas-Salcedo, et al., 2020; McCoy et al., 2022). In this study, we focus our analysis on how changes in extratropical moisture convergence contribute to SO SW_{FB}. As shown in Held and Soden (2006), column-integrated water vapor increases with warming following Clausius-Clapeyron scaling (C-C) (globally averaged rate about 7 $\%/K$). Two direct consequences of increased lower-tropospheric humidity are increased horizontal transport of water vapor and enhanced patterns of moisture convergence and divergence. The latter change also satisfies the C-C scaling, albeit with some adjustments in its spatial pattern such as the poleward expansion of subtropical drying (Siler et al., 2018; Bonan et al., 2023). Local precipitation and evaporation in the extratropics increase with warming but at a slower rate than C-C scaling owing to the energetic constraints (Allen & Ingram, 2002; Lorenz & DeWeaver, 2007; Stephens & Ellis, 2008; K. Trenberth, 2011). Thus, the convergence of moisture exceeds local evaporation and increases the extratropical moisture supply (K. E. Trenberth, 1998). Because the conversion of water vapor to precipitation happens in clouds, increases in both source and sink of clouds should guarantee an increase in extratropical cloudiness (McCoy et al., 2022). The negative SW_{FB} owing to increased liquid cloud condensates is most notable in the region where moisture convergence is increasing with warming, which tends to be poleward of 50^oS in the SO (Fig 1a and Fig S1). Here, we will investigate if changes in moisture flux can predict the SO LWP response to warming and in turn, how this affects the SO SW_{FB}. Spaceborne observations and reanalysis are used to constrain the SO SW_{FB}. We provide an outline of how we do this below.

SW_{FB} is the change in upwelling shortwave (SW) radiation fluxes ($SW_{\uparrow}$) at the top of atmosphere (TOA) due to adjustment of cloud properties and scaled by changes in GMT. Because downwelling SW radiation flux ($SW_{\downarrow}$) is a function of season and latitude, the local SW_{FB} should be proportional to the cloud-induced change in SW albedo ($\alpha = SW_{\uparrow}/SW_{\downarrow}$) scaled by GMT ($\partial\alpha_C/\partial GMT$) for a given time and latitude. In turn, the change in α can be expressed as the product of the susceptibility of α to liquid ($\partial\alpha/\partial LWP$) and the response of cloud liquid to warming ($dLWP/dGMT$)

$$SW_{FB} \propto \frac{\partial \alpha_C}{\partial GMT} \sim \frac{\partial \alpha}{\partial LWP} \cdot \frac{dLWP}{dGMT} \tag{1}$$

The change in α caused by ice is ignored for two reasons: First, the response of cloud ice is much smaller than response of liquid to global warming (McCoy et al., 2022), with a median ratio of changes in LWP to ice water path across GCMs of 8 (McCoy et al., 2016). Second, the reflectivity of SW radiation per unit mass of ice is typically less than that of liquid, owing to the smaller average size of liquid droplets (Liou, 2002; McCoy et al., 2014b). In Section 3.3 we evaluate the predictive ability of the right-hand side of Equation 1 in GCMs neglecting ice.

We constrain the SO SW_{FB} by providing constraints on each term on the right-hand side of Equation 1. Methods for computing the right-hand side of Equation 1 are discussed in section 2. LWP response to global warming is predicted using meteorological variability, discussed in detail in section 2.1 and 2.2. The method for estimating the radiative susceptibility is presented in section 2.3. Sections 2.4 and 2.5 describe how to compute these two terms from GCM data and observations, respectively. Section 3.1 provides observational constraints on the GCM LWP responses. Section 3.2 analyzes the opposing roles of radiative susceptibility and LWP response in setting the SO SW_{FB}. Section 3.3 produces a constraint on the SO SW_{FB} by splitting the LWP constraint into latitude bands consistent with regions of persistent drying and moistening. Conclusions are presented in section 4 with suggestions for future work.

2 Data and Methodology

2.1 Cloud-controlling Factor Analysis

In this study, we examine the linear relationships between large-scale environmental factors and clouds. The large-scale environmental factors that control local cloud processes are referred to as cloud-controlling factors (CCFs, Stevens and Brenguier (2009)). CCF analysis is based on the idea that response of local cloud properties to global warming can be expressed by a first-order Taylor expansion in CCFs (X_i) (Klein et al., 2017). CCF analysis allows us to use observations to constrain the response of LWP to to global mean temperature (GMT) (Qu et al., 2015). Following Qu et al. (2015), we predict the response of LWP to GMT as follows:

$$\begin{gathered}\frac{\Delta LWP}{\Delta GMT} = \sum \frac{\partial LWP}{\partial X_i}\frac{\Delta X_i}{\Delta GMT} + Res \\ X_i = \ T_s,\ P-E,\ LTS,\ \omega_{500}\end{gathered} \tag{2}$$

The LWP response GMT is decomposed into the LWP response to CCFs and a residual term. LWP response to GMT induced by each CCF is a product of the sensitivity of LWP to CCF ($\partial LWP/\partial X_i$) and the response of CCFs to changes in GMT ($\Delta X_i/\Delta GMT$). We constrain the LWP response to GMT by replacing the $\partial LWP/\partial X_i$ derived from GCMs with the observed sensitivities and estimating $\Delta X_i/\Delta GMT$ from GCMs' quadrupling CO_2 simulations. The constraint assumes that the sensitivities derived from present climate are applicable to predict future cloud change. This assumption requires an invariant relationship between local cloud properties and CCFs across any time scale greater than 2-3 days, which is the time scale that the boundary layer and its clouds can re-adjust to CCF changes (Schubert et al., 1979; Bretherton, 1993). This is referred to as "time-scale invariance" (Klein et al., 2017). We evaluate the time-scale invariance of our relationships between CCFs and LWP with an out-of-sample test from the observational record and an out-of-sample test from the GCM simulations. In section 3.1.1, we show that the observed sensitivities of LWP to CCFs derived from 2012−2016 monthly-mean data are able to predict the annual mean LWP change in the SO back to the early 1990s. For GCMs, section 3.1.2 shows the sensitivities computed using monthly preindustrial control ($piControl$) simulations are able to predict the long-term variation of LWP in 150 years of abrupt CO2 quadrupling ($abrupt4xCO_2$) simulations.

The CCFs considered in this study are surface skin temperature (T_s), precipitation minus evaporation ($P{-}E$), lower tropospheric stability (LTS) (Klein & Hartmann, 1993), and 500 mb subsidence (ω_{500}). These factors are consistent with McCoy, Field, Bodas-Salcedo, et al. (2020) and McCoy et al. (2022). Because GCMs do not output moisture convergence as a variable, we use $P{-}E$ as a proxy. These terms differ by the change in moisture storage over time (see Fig 1 in Seager and Henderson (2013)). Fig S2 shows $P{-}E$ is close to moisture convergence in the $40{-}85^oS$ region for ERA-5 reanalysis if we averaged the variables over a large spatial scale (5^o x 5^o). Seager and Henderson (2013) also states that the discrepancy between these two terms should be smaller in GCMs than in reanalysis because of the absence of an analysis increment in GCMs. For the above reasons, we average LWP and CCFs data into 5^o x 5^o gridboxes in the SO to make $P{-}E$ a reasonable approximation of moisture convergence. In this study, the LWP response is predicted on each 5^o x 5^o gridbox in the SO.

The moisture convergence is consistently positive across GCMs in the SO region in *picontrol* simulations (gray lines in Fig S1). In $abrupt4xCO_2$ simulations moisture convergence reduces in $40 - 50^oS$ region and enhances in $50 - 85^oS$ region (colored lines in Fig S1). This implies a poleward expansion of subtropical drying under global warming (Siler et al., 2018; Bonan et al., 2023) and is consistent with 50^oS acting as the demarcation between the positive SW_{FB} (negative $\Delta LWP/\Delta GMT$) region and negative SW_{FB} (positive $\Delta LWP/\Delta GMT$) region (Fig 1a) in GCMs driven by changes in moisture convergence. Following the regimes of persistent drying and moistening, SO LWP response and SW_{FB} are constrained in $40{-}50^oS$ and $50{-}85^oS$ regions in section 3.1.2 and 3.3.

2.2 Temperature Partitioning of Southern Ocean Clouds

CCF analysis has been used to predict the response of boundary layer cloud to warming in the tropics and subtropics (Qu et al., 2015; Zhai et al., 2015; Myers & Norris, 2016; Brient & Schneider, 2016; McCoy et al., 2017; Myers et al., 2021; Wall et al., 2022). The extratropical region presents a unique set of challenges in predicting the boundary layer cloud response to warming with a single set of linear relationships as in Equation 2. In the SO region, surface temperature varies from 210 K in the austral winter over the sea ice to around 290 K in the summer near 40^oS. The temperature of clouds over the ocean and sea ice varies along with the surface temperature. The wide temperature range in the SO results in a combination of mixed-phase and liquid-only boundary layer clouds. The formation and removal processes governing these cloud types are very different. The initial nucleation and growth processes happen at different rates in mixed-phase ($T < 0^oC$) and liquid-only ($T > 0^oC$) clouds (Jeffery & Austin, 1997; Koop et al., 2000; Schaller & Fukuta, 1979; Mossop, 1985; Lamb & Verlinde, 2011). Precipitation efficiency is higher in mixed-phase clouds than in liquid-only clouds due to the rapid growth of ice crystals at the expense of liquid drops (Wegener-Bergeron-Findeisen (WBF) process) (Storelvmo & Tan, 2015). The higher precipitation efficiency of mixed-phase clouds results in the majority of mid-latitude precipitation events originating as snow (Field & Heymsfield, 2015).

Previous studies suggest that mixed-phase and liquid-only clouds respond differently to global warming. Gordon and Klein (2014) shows that low cloud optical depth increases with warming for cold clouds and decreases with warming for warm clouds in GCMs. This behavior is also found by in-situ observations (Terai et al., 2019). These studies state that the increase of cold cloud optical depth is due to the increased cloud water content, while the decrease of warm cloud optical depth is owing to reduced cloud physical thickness. In addition to these mechanisms, analysis of GCMs has suggested that phase changes in mixed-phase clouds in response to warming are important to the accurate representations of SW_{FB} and ECS (Tan et al., 2016; Bjordal et al., 2020).

Because of the strongly differing cloud physics and response behaviors of warm and cold clouds, we treat them separately by splitting our analysis into two CCF models. We characterize cold and warm clouds in the SO by T_s. Each 5^o x 5^o gridbox in $40{-}85^oS$ is counted as the cold (warm) regime if the T_s of this gridbox is lower than (larger or equal to) a threshold T_s (TR_{T_s}). This results in two CCF models split over TR_{T_s}:

$$
\begin{aligned}
\frac{\Delta LWP}{\Delta GMT}|_{Cold} &= \sum \left(\frac{\partial LWP}{\partial X_i}|_{Cold} \cdot \frac{\Delta X_i}{\Delta GMT}|_{Cold}\right) + Res_1 \\
T_s &< TR_{T_s} \\
\frac{\Delta LWP}{\Delta GMT}|_{Warm} &= \sum \left(\frac{\partial LWP}{\partial X_i}|_{Warm} \cdot \frac{\Delta X_i}{\Delta GMT}|_{Warm}\right) + Res_2 \\
T_s &\geq TR_{T_s}
\end{aligned} \tag{3}
$$

For each GCM, TR_{T_s} is the temperature that maximizes the explained variance of GCM LWP by Equation 3. We iterate through potential values of TR_{T_s} from 210 K to 290 K. For each potential TR_{T_s}, the r^2 of Equation 3 trained by *picontrol* simulations is computed. Fig 2 shows the r^2 for each GCM as a function of potential TR_{T_s} in *piControl* simulations. The TR_{T_s} for most GCMs is around 270 K, which generally separates the clouds over sea ice from the warm open ocean. This is consistent with other studies showing minimal supercooled liquid fraction in GCMs when cloud temperature is lower than 255 K (Komurcu et al., 2014). If we assume a typical lapse rate of $6.5K/km$ and cloud height of $2-3$ km in the extratropical environment, this is consistent with a surface temperature of 270 K. The TR_{T_s} and resultant regime-specific $\partial LWP/\partial X_i$ derived from *piControl* simulations are used to partition the regimes and predict the LWP response to warming in $abrupt4xCO_2$ simulations. Fig S3 shows that the TR_{T_s} trained by $abrupt4xCO_2$ simulations are qualitatively the same as the mean-state values.

Because microwave radiometers do not retrieve LWP over sea ice (Elsaesser et al., 2017), it is hard to do the same cold-warm partitioning in observations. The lack of high-latitude LWP data in the SO limits the possible range of TR_{T_s} derived from observations, and they do not significantly improve predictions as in GCMs shown in Fig 2. For this reason, the observed SO is only treated as a single regime. In section 3.1.1, we evaluate whether our prediction of observed LWP is degraded by only using the single regime CCF model Equation 2.

2.3 Radiative Susceptibility

In Equation 1, the response of LWP to GMT is connected to its SW radiative effect through a radiative susceptibility term ($\partial\alpha/\partial LWP$). This term describes how a change in LWP affects α while keeping other factors fixed. Following McCoy et al. (2022), the radiative susceptibility is estimated by training the multi-linear regression model:

$$\alpha = c_1 * LWP + c_2 * \alpha_{clear-sky} + c_3; \tag{4}$$

where c_1 is $\partial\alpha/\partial LWP$. α is a function of clear-sky albedo (α_{cs}) and LWP, which is in turn affected by cloud areal extent (Bender et al., 2017) and cloud optical depth (Gordon & Klein, 2014). To reduce the effects introduced by the seasonal cycle of solar zenith angle (SZA), we only train Equation 4 on January data, during which time the SZA is smallest and the effect of cloud properties on α is most pronounced (see Fig 2 in McCoy et al. (2018) for the relationships between α, cloud fraction, and SZA). The effects of high α_{cs} is excluded in our analysis by threshold ($TR_{\alpha_{cs}}$). We test a series of $TR_{\alpha_{cs}}$ in section 3.2 to estimate whether c_1 is sensitive to this threshold. Removing high α_{cs} removes data over sea ice from the models, making this calculation analogous to the observations where retrievals are not available over sea ice. The regression model is trained on data from the SO region at the native spatial resolution of each GCM and of observations.

2.4 Global Climate Models

We compute the LWP response to GMT of GCMs by using monthly-mean output from the mean-state (*piControl*) and the quadrupling CO_2 ($abrupt4xCO_2$) simulations from 50 GCMs participating in CMIP5 (20) and CMIP6 (30). GCMs used in this study are listed in Table S1.

Radiative susceptibility ($\partial\alpha/\partial LWP$) is computed using *piControl*. The CCF model (Equation 3) is trained on *piControl* output to calculate regime-specific sensitivities of LWP to CCFs ($\partial LWP/\partial X_i$). Changes in CCFs scaled by GMT ($\Delta X_i/\Delta GMT$) are computed as the differences between the *piControl* average and the 121 - 140 year mean of $abrupt4xCO_2$ simulations following Myers et al. (2021). Following Equation 3, these terms are combined to predict $\Delta LWP/\Delta GMT$. The time-scale invariance of Equation 3 is evaluated by comparing $\Delta LWP/\Delta GMT$ predicted from Equation 3 to $\Delta LWP/\Delta GMT$ calculated from GCM output.

LWP is the column-integrated liquid water mass, computed by using *clwvi* (total condensed water path for liquid and ice) minus *clivi* (ice water path). Monthly-mean LWP for GCM is averaged over the cloudy and cloud-free portion of the model gridbox, which is consistent with the microwave LWP retrieval used in this study (section 2.5). The following variables are used for CCFs (X_i): *ts* for surface temperature; *pr* and *hfls* for precipitation and evaporation; *ta* at 700 mb, *ps*, and *ts* for lower tropospheric stability and *wap* at 500 mb for subsidence. The radiative susceptibilities ($\partial\alpha/\partial LWP$) of GCMs are computed by regressing the SW albedo ($\alpha = rsut/rsdt$) on clear-sky albedo ($\alpha_{cs} = rsutcs/rsdt$) and LWP.

2.5 Observations

Observations of monthly-mean cloud LWP are provided by the Multisensor Advanced Climatology of Liquid Water Path (MAC-LWP) data set (Elsaesser et al., 2017; O'Dell et al., 2008). MAC-LWP synthesizes microwave LWP observations from multiple satellites. Cloud LWP is the liquid water mass within an atmospheric column excluding precipitating liquid. The monthly-mean LWP is averaged over the cloudy and cloud-free scenes of each 1^o x 1^o gridbox. Microwave observations of LWP are only available over the open ocean. Modern-Era Retrospective analysis for Research and Applications, Version 2 (MERRA-2) reanalysis (Gelaro et al., 2017) is used to describe CCFs. MAC-LWP LWP and MERRA-2 CCFs from 1992 to 2016 are used to conduct the out-of-sample test in section 3.1.1 and provide constraints on GCM LWP responses in section 3.1.2. LWP and CCFs are binned into the same 5^o x 5^o averages used in the analysis of GCM output.

A missing data threshold of 50% is used in each 5^o x 5^o gridbox. Fig 3 compares the fraction of gridboxes with sufficient data to the fraction of warm regime gridboxes for 50 GCMs. The distribution of observations in SO is qualitatively close to the warm regime of GCMs. Since most of the GCMs group all open water into one regime ($TR_{T_s} \approx 270\ K$), the observed SO becomes an approximation to the GCM warm regimes. Because of this, a CCF model with only one regime (Equation 2) is used to predict the historical record of LWP in section 3.1.1. The derived $\partial LWP/\partial X_i$ from observations is used to constrain the warm regime LWP response to GMT in GCMs. The propagation of the constraint range from the warm regime to the entire SO is discussed in section 3.1.2.

Equation 4 is used to calculate $\partial\alpha/\partial LWP$ from monthly-mean TOA shortwave fluxes from the Clouds and the Earth's Radiant Energy System (CERES) EBAF-TOA data (Ed 4.1) (Loeb et al., 2018; Wielicki et al., 1996) combined with LWP from MAC-LWP. Observations from 2003 to 2016 are used. This period is set by the availability of CERES and MAC-LWP data.

3 Results

3.1 Prediction of LWP

To constrain SW_{FB} using Equation 1, we need to constrain the response of SO LWP to warming. To do this, we need to evaluate whether the sensitivity of LWP to CCFs is time-scale invariant (Klein et al., 2017). We examine time-scale invariance using two out-of-sample tests. First, we evaluate whether the regression model in Equation 2 trained on a short period of observations can predict past variations of LWP. This is shown in section 3.1.1. Second, we evaluate whether the regression model in Equation 3 trained on the mean-state climate from GCMs can predict the LWP response to a quadrupling in CO2. This is discussed in section 3.1.2. Following these tests, we use observations to constrain the spread of GCM LWP responses to GMT in $abrupt4xCO_2$ simulations in section 3.1.2 and discuss the contribution of CCFs to LWP response to GMT in section 3.1.3.

3.1.1 Historical Trends in LWP

We split the observations of LWP and reanalysis of CCFs from 1992 to 2016 into a training period (2012 - 2016) and a validation period (1992 - 2011). We train the sensitivities of LWP to CCFs ($\partial LWP/\partial X_i$) using monthly-mean observational data in the training period and use them to predict the annual variation of LWP in the validation period. Fig 4a shows the decadal trend in SO LWP from MAC-LWP observation and the prediction of Equation 2. MAC-LWP shows a positive trend of LWP in the past two decades, consistent with Manaster et al. (2017). The predicted LWP by Equation 2 broadly reproduces the positive trend of LWP during this period from 1996 until 2012. Before 1996, the predicted LWP trend appears to reverse. This may be because the meteorological predictors used in the regression model are reliant on the observations being ingested in MERRA-2. Many fewer observations of precipitation are available before the mid-1990s (Gelaro et al., 2017). The lack of observational input to reanalysis may lead to the disagreement between the Equation 2 predicted LWP and observations in the early 1990s. The ability of Equation 2 to predict decadal-scale trends in LWP in an out-of-sample test supports the time scale invariance of $\partial LWP/\partial X_i$ derived from observations. Our choice of training and validation period does not substantiall affect the ability of the CCF model to predict LWP (Fig S4).

Fig 4b shows the decomposition of LWP response into contributions from individual CCFs. The positive trend in SO LWP can be largely explained by the changes in $P-E$. Increases in surface temperature explain only a small fraction of the LWP trend. Stability and large-scale subsidence have negligible effects on the SO LWP on a decadal scale. Increased $P-E$ is related to the increased moisture content in the extratropical atmosphere. This result suggests the important role of hydrological response to the observed LWP increase in the SO for the past two decades.

3.1.2 Predicting LWP response to CO2 Quadrupling

Following our evaluation of whether Equation 2 can predict the observed decadal variability of LWP, we evaluate whether Equation 3 trained on mean-state ($piControl$) output can predict the response of LWP to CO2 quadrupling ($abrupt4xCO_2$). Fig 5 shows the predicted LWP change scaled by GMT change ($\Delta LWP/\Delta GMT$) between the $piControl$ average and the 121 - 140 years mean of $abrupt4xCO_2$ simulations. The 50 GCMs shown are from CMIP5 and CMIP6 and are listed in Table S1. LWP response to GMT is shown separated into three different latitude bands: $40{-}85^oS$ (Fig 5ab); $40{-}50^oS$ (Fig 5cd); and $50-85^oS$ (Fig 5ef). The $40-50^oS$ and $50-85^oS$ correspond to the regions of drying and moistening in response to warming (Fig S1). As discussed in section 2.5, observational constraint from MAC-LWP is only available in the warm regime. Latitudinal-averaged $\Delta LWP/\Delta GMT$ in the warm regime is shown in Fig 5ace. Latitudinal-averaged $\Delta LWP/\Delta GMT$ for both regimes is shown in Fig 5bdf.

Equation 3 explains 70% of the variance in $40{-}85^oS$ $\Delta LWP/\Delta GMT$across GCMs (Fig 5b). The best fit line between the CCF model predictions and the actual GCM output is close to 1-1 line. This result supports the time-scale invariant relationships between LWP and CCFs in Equation 3. The explained variance in $\Delta LWP/\Delta GMT$ by Equation 3 is 59% averaged over $40{-}50^oS$ (Fig 5d). This decrease in explained variance may be related to the hydrological response in this region. While moisture convergence is positive in $40{-}50^oS$ in the mean-state climate, this pattern becomes less robust at the end of $abrupt4xCO_2$ simulations with some GCMs displaying drying and some displaying moistening (Fig S1). In the $50{-}85^oS$ latitude band, explained variance in $\Delta LWP/\Delta GMT$ is 86% (Fig 5f).

To provide observational constraints on $\Delta LWP/\Delta GMT$ in these three latitude bands, we need to evaluate the amount of constraint provided by the warm component of Equation 3 because observations are only available in this regime. Fig 5ace display the constraint range of warm regime $\Delta LWP/\Delta GMT$ in each latitude band as red shading on the x-axis. These constraints are obtained by replacing the GCM $\partial LWP/\partial X_i$ in the warm regime with $\partial LWP/\partial X_i$ computed from observations in section 3.1.1. The warm regime explains a large fraction of variance in $\Delta LWP/\Delta GMT$ across GCMs for all latitude bands (see r^2 in Fig 5ace). The variance in $\Delta LWP/\Delta GMT$ averaged over $40{-}85^oS$ explained by the warm regime is high ($r^2 = 0.88$, Fig 5a). Only the warm regime exists in the $40-50^oS$ region and $r^2 = 1$ (Fig 5c). The explained variance in $\Delta LWP/\Delta GMT$ is still relatively high in the $50-85^oS$ region ($r^2 = 0.67$, Fig 5e).

We propagate the observational constraint from the warm regime to latitudinal-averaged $\Delta LWP/\Delta GMT$. This is done using the linear relationships in Fig 5ace. Uncertainty in the fit is estimated by Jackknife resampling (Tukey, 1958). We intersect the shaded region on the x-axis of Fig 5ace with the best fit line and uncertainty to propagate our constraint from the warm regime to the sum of warm and cold regimes in each latitude band. In Fig 5bdf, the constraints from the y-axis of 5ace are shown as the brown shading on the x-axis. The fit lines in Fig 5bdf are used to propagate the constraints on the CCF model predictions to the GCM LWP response. These constraints are used in section 3.3 to constrain SW_{FB}.

3.1.3 CCF Contributions to LWP Response to CO2 Quadrupling

In this section we show the sensitivities of LWP to CCFs ($\partial LWP/\partial X_i$) and each CCFs contribution to the response of LWP to warming ($\Delta LWP/\Delta GMT$). Values of $\partial LWP/\partial X_i$ for each GCM is shown in Fig 6a. The change in each CCF between $picontrol$ and $abrupt4xCO_2$ simulations is shown in Fig 6b. Following Equation 3, the product of these two terms is the contribution of each CCF to $\Delta LWP/\Delta GMT$ (Fig 6c). Cold and warm regime values are shown in each subplot separately. Observed $\partial LWP/\partial X_i$ are displayed for the warm regime (Fig 6a).

The dependence of LWP on CCFs across GCMs and observations is broadly consistent with previous studies (Fig 6a). The dependence of LWP on T_s is positive across all the GCMs for the cold regime but with less agreement in the sign for the warm regime. This is consistent with previous studies suggesting cold cloud optical depth will increase with temperature (Gordon & Klein, 2014; Terai et al., 2019), mostly due to the increased cloud water content (Betts & Harshvardhan, 1987). Terai et al. (2019) suggests that the cloud optical depth for warm clouds may decrease or stay constant with increasing temperature owing to the reduced cloud adiabaticity. The dependence of LWP on $P-E$ is positive for warm and cold regimes, which is consistent with previous literature (McCoy et al., 2019; McCoy, Field, Gordon, et al., 2020). The dependence of LWP on LTS is mostly positive in the warm regime of GCMs, while the sensitivity of LWP to ω_{500} is small. This is consistent with previous work on boundary layer cloudiness (Zelinka et al., 2018; Myers & Norris, 2015, 2013). The observed sensitivities of LWP to T_s and $P{-}E$ are positive and much larger than the LTS and ω_{500} sensitivities.

Both T_s and $P-E$ increase with warming in warm and cold regimes (Fig 6b). LTS increases with warming in the warm regime but decreases in the cold regime. This robust pattern may be related to the poleward shift of the Hadley cell (stabilizing the warm regime lower troposphere) and the poleward shift of the Southern Hemisphere storm track (destabilizing the cold regime lower troposphere) simulated by GCMs (Barnes & Polvani, 2013; Bender et al., 2012). The change in large-scale subsidence is relatively small compared with other CCFs.

Combining $\partial LWP/\partial X_i$ and the response of CCF to warming ($\Delta X_i/\Delta GMT$) allows us to apportion $\Delta LWP/\Delta GMT$ among CCFs (Fig 6c). In the warm regime, GCMs have roughly equivalent contributions due to surface temperature, moisture convergence, and stability. In the cold regime, moisture convergence and surface temperature changes contribute the most.

Among the GCMs surveyed here (Table S1), the second Community Earth System Model (CESM2, Danabasoglu et al. (2020)) and its variants (CESM2-FV2, CESM2-WACCM, CESM2-WACCM-FV2, and E3SM-1-0) in CMIP6 predict a decrease in LWP after the first 15 years in $abrupt4xCO_2$ simulations (Bjordal et al., 2020; McCoy et al., 2022). This is shown in Fig 1b where these models display a non-monotonic response of LWP to GMT. These models also report the most positive extratropical SW_{FB} (Fig 1a) and the highest ECS among GCMs (Table S1). We single out CESM2 in Fig 6. The prediction of CESM2 LWP response to warming by the CCF model is not as accurate as other GCMs (Fig S5). However, it is substantially improved from McCoy et al. (2022) (CESM2 is much closer to the 1-1 line in Fig 5b compared to Fig 2 in McCoy et al. (2022)). While more work is needed to more accurately predict CESM2 LWP response to warming using a CCF model, the near-zero change in LWP from *piControl* to the end of the $abrupt4xCO_2$ simulations in the warm regime is captured by the CCF model (Fig 6c and Fig S5). Fig 6 suggests that the LTS-induced increase in LWP in the warm regime is offset by decreases related to T_s. CESM2 displays the lowest sensitivity of warm regime LWP to $P{-}E$ and the $P{-}E$ contribution to LWP response is small. Observational constraint suggests that CESM2 overestimates the LTS sensitivity and underestimates the $P{-}E$ sensitivity in the warm regime. The dependence of LWP to T_s in the warm regime is negative in CESM2 but is positive from observations (Fig 6a). Because of the positive changes in T_s, $P{-}E$, and LTS in response to warming in the warm regime (Fig 6b), the overall effect is the near-zero response of LWP in CESM2 in the $abrupt4xCO_2$ simulation.

3.2 Radiative Susceptibility

Following Equation 1, SW_{FB} is proportional to the product of changes in LWP and the sensitivity of albedo to the changes in LWP. The radiative susceptibility ($\partial\alpha/\partial LWP$) is computed for each GCM and from observations. Across GCMs, $\partial\alpha/\partial LWP$ varies by nearly a factor of seven. One emergent behavior in GCMs is an inverse relationship between $\partial\alpha/\partial LWP$ and mean-state LWP (Fig 7). This is consistent with previous studies (McCoy et al., 2022). α and cloud fraction (areal coverage of clouds) are approximately linearly related (Bender et al., 2017). However, the effect of $LWP_{in-cloud}$ on albedo saturates at high $LWP_{in-cloud}$ (Lacis & Hansen, 1974). The SO mean-state LWP is a function of cloud fraction and $LWP_{in-cloud}$. A GCM that simulates high mean-state LWP would have fewer clear-sky pixels that could be filled in the warmed climate and is closer to radiative saturation. As LWP increases with warming, additional liquid affects α less efficiently by only increasing the in-cloud liquid rather than increasing cloud coverage.

Observed radiative susceptibility trained on CERES and MAC-LWP is also shown in Fig 7. One potential source of uncertainty in estimating $\partial\alpha/\partial LWP$ is the clear-sky α threshold ($TR_{\alpha_{cs}}$) applied in Equation 4. We show this uncertainty in the SW_{FB} constraint by examining a range of observed $\partial\alpha/\partial LWP$ computed using $TR_{\alpha_{cs}}$ from 0.11 to 0.30. The $\partial\alpha/\partial LWP$ derived from observations is on the low end of the GCM distribution even accounting for this uncertainty in observations and GCMs. This result suggest that the too-bright and too-homogeneous bias of tropical clouds in CMIP6 GCMs may also exist in the simulation of extratropical clouds (Konsta et al., 2022).

The sensitivity of LWP to moisture convergence ($\partial LWP/\partial P - E$) positively correlates with mean-state LWP in both cold and warm regime (Fig 7). This relationship can be explained in the context of sources and sinks of cloud liquid content (McCoy et al., 2022). Source and sink rates of clouds can be written as:

$$\begin{aligned} K_{source} &= e_{source} \cdot r_{water\ vapor} \\ K_{sink} &= e_{sink} \cdot r_{LWP} \end{aligned} \tag{5}$$

the product of a bulk efficiency of sources (e_{source}) and sinks (e_{sink}) of cloud liquid with their respective reservoir terms. The reservoir that liquid draw from is water vapor ($r_{water\ vapor}$) and the reservoir of the sink of liquid in this model is cloud liquid itself (r_{LWP}). In the mean-state climate, sources and sinks are balanced ($K_{source} = K_{sink}$) and

$$\frac{e_{source}}{e_{sink}} = \frac{r_{LWP}}{r_{water\ vapor}}. \tag{6}$$

Following this model, mean-state LWP is proportional to the relative strength of source and sink efficiencies (i.e., e_{source}/e_{sink}). If we assume the same water vapor ($r_{water\ vapor}$) in the mean-state climate in GCMs, the diversity in model mean-state LWP can be traced back to the subgrid-scale parameterization of cloud source and sink processes. We note that the similar water vapor amount is only an assumption as free-running models without a fixed SST will result in slightly different mean-state water vapor paths (Jiang et al., 2012). In this simple model, the sensitivity of LWP to moisture convergence ($\partial LWP/\partial P - E$) trained using GCM mean-state climate may act as a proxy of this relative strength of source to sink efficiencies ($e_{source}/e_{sink} \propto \partial LWP/\partial P - E$).

The steady-state framework presented above may help us understand why $\partial LWP/\partial P - E$ in the cold regime is consistently larger than the value in the warm regime (Fig 7). In this framework, it is because of a stronger source efficiency for cold regime clouds due to the larger moist adiabat (Betts & Harshvardhan, 1987), even though the sink efficiency for cold regime clouds is likely to be larger as well (Field & Heymsfield, 2015).

How does this steady-state framework inform us about the diversity in the response of LWP to warming? The moisture content ($r_{water\ vapor}$) in extratropics increases with GMT. If we assume the relative strength of source to sink efficiency (e_{source}/e_{sink}) is fixed under climate change, a model with larger mean-state sensitivity of LWP to $P{-}E$ would lead to a larger increase in LWP. The warm regime $\partial LWP/\partial P - E$ and $\Delta LWP/\Delta GMT$ covary across GCMs (Fig S6) with a correlation of $r = 0.78$.

3.3 Constraints on Southern Ocean SW Cloud Feedback

In the proceeding section, we examine the response of SO LWP to GMT predicted by CCFs and the response of α to LWP in order to predict SW_{FB} (Equation 1). Based on the observational constraints on $\Delta LWP/\Delta GMT$ in Fig 5 and the observational constraint on $\partial\alpha/\partial LWP$ in Fig 7, we provide constraints on SW_{FB} in Fig 8. Equation 1 explains 53 % and 52 % of the variance in GCM SW_{FB} averaged over $40-50^oS$ and $50{-}85^oS$ regions, respectively (Fig 8). Observational constraints on the right-hand side of Equation 1 predict the contributions to global mean SW_{FB} from $40{-}50^oS$ and $50{-}85^oS$ regions to be $-0.04{-}0.06\ W\ m^{-2}\ K^{-1}$ and $-0.15{-}0.01\ W\ m^{-2}\ K^{-1}$. The latter range is consistent with the $50-85^oS$ constraint range ($-0.10-0.0\ W\ m^{-2}\ K^{-1}$) reported by McCoy et al. (2022). These ranges are calculated by taking the shaded y-ranges in Fig 8 and scaling them by the ratio of the area in the latitude band to global area. The uncertainties in $40-50^oS$ and $50-85^oS$ SW_{FB} constraints are calculated by combining uncertainties in the observational constraint on $\Delta LWP/\Delta GMT$ (see section 3.1.2 for details of uncertainty propagation) and uncertainties in $\partial\alpha/\partial LWP$ (the observational uncertainty owing to α_{cs} threshold). The constraint on $40{-}50^oS$ is tighter than $50-85^oS$ because observational constraint on $\Delta LWP/\Delta GMT$ is only available in the warm regime and the $40-50^oS$ region is entirely warm regime.

We combine our constraints on SW_{FB} in the $40-50^oS$ and $50-85^oS$ latitude bands to compute the constraint on $40-85^oS$ SW_{FB}. The distributions of $40-50^oS$ and $50-85^oS$ SW_{FB} located in the constraint ranges on the x-axis of Fig 8 are normally distributed. We take the sum of the area-weighted latitudinal constraints in $40{-}50^oS$ and $50{-}85^oS$ and propagate their standard errors to estimate $40{-}85^oS$ SW_{FB}. The contribution of the SO ($40{-}85^oS$) to the global mean SW_{FB} is constrained as $-0.19{-}0.05\ W\ m^{-2}\ K^{-1}$ at 95% confidence interval (Fig 9). This range is a bit wider than the range reported by McCoy et al. (2022), but we have added a new constraint from $40{-}50^oS$ latitude band and taken into account the uncertainty owing to different α_{cs} thresholds.

4 Conclusions

In this work, we built a Cloud Controlling Factor (CCF) regression model to predict the response of the Southern Ocean (SO, $40-85^oS$) LWP. The CCFs considered in the regression model were surface temperature (T_s), precipitation minus evaporation ($P{-}E$, approximately the moisture convergence), lower tropospheric stability (LTS), and 500 mb subsidence (ω_{500}). Warm and cold clouds are regulated by very different microphysical processes and have different responses to warming. To allow the CCF regression model to adapt to this, we partitioned the SO into cold and warm regimes. This new method increases the robustness of the CCF model prediction compared to previous work (McCoy et al., 2022). We used two out-of-sample tests to evaluate the predictive ability of our CCF regression model: the ability of our CCF model trained on observations to replicate the observed decadal trend in SO LWP (section 3.1.1, Fig 4) and the ability of our CCF model trained on the mean-state output of GCMs to predict their response to CO_2 quadrupling (section 3.1.2, Fig 5). Using the CCF regression model trained on observations combined with the GCM simulated changes in CCFs in response to CO_2 quadrupling, we were able to provide an observational constraint on the change in LWP in response to GMT ($\Delta LWP/\Delta GMT$) of $2.89\ -\ 4.41\ gm^{-2}K^{-1}$ (Fig 5b).

Ultimately, the quantity we care about in relation to Earth's radiation budget is not cloudiness, but radiative flux. We define a radiative susceptibility metric ($\partial\alpha/\partial LWP$) that we can use to scale our constrained LWP response. We computed $\partial\alpha/\partial LWP$ from satellite observations and GCM output. The observational constraint suggest that most of the GCMs overestimate $\partial\alpha/\partial LWP$ (Fig 7), which is consistent with recent studies of tropical clouds (Konsta et al., 2022). Satellite observations estimate $\partial\alpha/\partial LWP$ to be $0.41 - 0.86$ $(kg\ m^{-2})^{-1}$.

GCMs with higher mean-state LWP tend to have lower $\partial\alpha/\partial LWP$ (Fig 7). This can be connected to the sensitivity of LWP to moisture convergence ($\partial LWP/\partial P - E$). GCMs with higher $\partial LWP/\partial P - E$ simulate higher mean-state LWP. These GCMs will tend to predict a larger LWP response ($\Delta LWP/\Delta GMT$) but have a lower $\partial\alpha/\partial LWP$ due to radiative saturation. This results in compensation between the LWP response to warming and the radiative susceptibility.

The product of $\partial\alpha/\partial LWP$ and $\Delta LWP/\Delta GMT$ predicts roughly 50 % of the variance in SO SW_{FB} across 50 CMIP5 and CMIP6 GCMs (Fig 8). Observational constraints on $\Delta LWP/\Delta GMT$ and $\partial\alpha/\partial LWP$ produce a constrained range on SO SW_{FB} of -0.19 to 0.05 $Wm^{-2}K^{-1}$ (95% confidence interval) (Fig 9), which suggest a moderate negative to weak positive SO SW_{FB}. This is consistent with previous work, but expands the constraint region to the entire SO as opposed to just constraining the region where GCMs consistently moisten (McCoy et al., 2022).

Our analysis suggests some directions of future studies seeking to constrain the extratropical SW_{FB}:

1. Our analysis identified increased moisture convergence into the SO as a key driver of increased LWP. This mechanism ultimately links the global circulation and hydrological cycle to the extratropical SW_{FB}. To better understand this linkage, it would be useful to understand how Hadley cell expansion and transient eddies (i.e. atmospheric rivers) contribute to long-term variability of the SO moisture budget.
2. Due to the lack of microwave observations of LWP over sea ice, we cannot provide an observations-constrained CCF model for the cold regime. In this study, the GCM relationship between the warm regime LWP response and the response averaged over the latitude band is used to fill the gap. Ground-based LWP observations in high latitude SO, such as those taken during the Atmospheric Radiation Measurement (ARM) West Antarctic Radiation Experiment (AWARE, Lubin et al. (2020)), may be able to provide an observational constraint on the cold regime LWP response.
3. We found that $\partial\alpha/\partial LWP$ varied dramatically across GCMs and strongly modulated the effect of changes in LWP on radiation. We also found that observations suggested that GCMs tended to have a $\partial\alpha/\partial LWP$ that was too large. One possibility is that this is due to clouds that are too uniform and radiatively efficient (Konsta et al., 2022; Nam et al., 2012). Determining the origin of this behavior might be helpful in identifying a potential source of GCM bias in SW_{FB}.

5 Open Research

GCM output used in this study are available from Earth System Grid Federation (ESGF) esgf-node.llnl.gov. MAC-LWP and MERRA-2 reanalysis data are available from the Goddard Earth Sciences Data and Information Services Center at disc.gsfc.nasa.gov. CERES data is available from ceres.larc.nasa.gov.

Acknowledgments

The efforts of CT, DTM, and GSE are supported under NASA-PMMST Grant #80NSSC22K0599. GSE acknowledges additional support from the NASA Modeling, Analysis and Prediction Program and APAM GISS Co-Op #80NSSC18M0133.

References

Allen, M. R., & Ingram, W. J. (2002, September). Constraints on future changes in climate and the hydrologic cycle. *Nature*, *419*(6903), 224–232. Retrieved 2023-02-27, from https://www.nature.com/articles/nature01092 doi: 10.1038/nature01092

Barnes, E. A., & Polvani, L. (2013, September). Response of the Midlatitude Jets, and of Their Variability, to Increased Greenhouse Gases in the CMIP5 Models. *Journal of Climate*, *26*(18), 7117–7135. Retrieved 2023-01-31, from http://journals.ametsoc.org/doi/10.1175/JCLI-D-12-00536.1 doi: 10.1175/JCLI-D-12-00536.1

Bender, F. A.-M., Engström, A., Wood, R., & Charlson, R. J. (2017, June). Evaluation of Hemispheric Asymmetries in Marine Cloud Radiative Properties. *Journal of Climate*, *30*(11), 4131–4147. Retrieved 2022-06-14, from http://journals.ametsoc.org/doi/10.1175/JCLI-D-16-0263.1 doi: 10.1175/JCLI-D-16-0263.1

Bender, F. A.-M., Ramanathan, V., & Tselioudis, G. (2012, May). Changes in extratropical storm track cloudiness 1983–2008: observational support for a poleward shift. *Climate Dynamics*, *38*(9-10), 2037–2053. Retrieved 2022-04-04, from http://link.springer.com/10.1007/s00382-011-1065-6 doi: 10.1007/s00382-011-1065-6

Betts, A. K., & Harshvardhan. (1987). Thermodynamic constraint on the cloud liquid water feedback in climate models. *Journal of Geophysical Research*, *92*(D7), 8483. Retrieved 2022-05-20, from http://doi.wiley.com/10.1029/JD092iD07p08483 doi: 10.1029/JD092iD07p08483

Bjordal, J., Storelvmo, T., Alterskjær, K., & Carlsen, T. (2020, November). Equilibrium climate sensitivity above 5 °C plausible due to state-dependent cloud feedback. *Nature Geoscience*, *13*(11), 718–721. Retrieved 2022-05-20, from https://www.nature.com/articles/s41561-020-00649-1 doi: 10.1038/s41561-020-00649-1

Bonan, D. B., Siler, N., Roe, G. H., & Armour, K. C. (2023, February). Energetic constraints on the pattern of changes to the hydrological cycle under global warming. *Journal of Climate*, 1–48. Retrieved 2023-02-24, from https://journals.ametsoc.org/view/journals/clim/aop/JCLI-D-22-0337.1/JCLI-D-22-0337.1.xml doi: 10.1175/JCLI-D-22-0337.1

Bretherton, C. S. (1993, July). Understanding Albrecht's Model of Trade Cumulus Cloud Fields. *Journal of the Atmospheric Sciences*, *50*(14), 2264–2283. Retrieved 2023-03-17, from http://journals.ametsoc.org/doi/10.1175/1520-0469(1993)050<2264:UAMOTC>2.0.CO;2 doi: 10.1175/1520-0469(1993)050⟨2264:UAMOTC⟩2.0.CO;2

Brient, F., & Schneider, T. (2016, August). Constraints on Climate Sensitivity from Space-Based Measurements of Low-Cloud Reflection. *Journal of Climate*, *29*(16), 5821–5835. Retrieved 2023-01-22, from http://journals.ametsoc.org/doi/10.1175/JCLI-D-15-0897.1 doi: 10.1175/JCLI-D-15-0897.1

Ceppi, P., Hartmann, D. L., & Webb, M. J. (2016, January). Mechanisms of the Negative Shortwave Cloud Feedback in Middle to High Latitudes. *Journal of Climate*, *29*(1), 139–157. Retrieved 2023-02-22, from http://journals.ametsoc.org/doi/10.1175/JCLI-D-15-0327.1 doi: 10.1175/JCLI-D-15-0327.1

Ceppi, P., McCoy, D. T., & Hartmann, D. L. (2016, February). Observational evidence for a negative shortwave cloud feedback in middle to high latitudes. *Geophysical Research Letters*, *43*(3), 1331–1339. Retrieved 2023-02-04, from https://onlinelibrary.wiley.com/doi/10.1002/2015GL067499 doi: 10.1002/2015GL067499

Danabasoglu, G., Lamarque, J., Bacmeister, J., Bailey, D. A., DuVivier, A. K., Edwards, J., … Strand, W. G. (2020, February). The Community Earth System

Model Version 2 (CESM2). *Journal of Advances in Modeling Earth Systems*, *12*(2). Retrieved 2023-03-30, from https://onlinelibrary.wiley.com/doi/10.1029/2019MS001916 doi: 10.1029/2019MS001916

Elsaesser, G. S., O'Dell, C. W., Lebsock, M. D., Bennartz, R., Greenwald, T. J., & Wentz, F. J. (2017, December). The Multisensor Advanced Climatology of Liquid Water Path (MAC-LWP). *Journal of Climate*, *30*(24), 10193–10210. Retrieved 2022-09-06, from https://journals.ametsoc.org/doi/10.1175/JCLI-D-16-0902.1 doi: 10.1175/JCLI-D-16-0902.1

Field, P. R., & Heymsfield, A. J. (2015, November). Importance of snow to global precipitation. *Geophysical Research Letters*, *42*(21), 9512–9520. Retrieved 2023-03-22, from https://onlinelibrary.wiley.com/doi/10.1002/2015GL065497 doi: 10.1002/2015GL065497

Gelaro, R., McCarty, W., Suárez, M. J., Todling, R., Molod, A., Takacs, L., ... Zhao, B. (2017, July). The Modern-Era Retrospective Analysis for Research and Applications, Version 2 (MERRA-2). *Journal of Climate*, *30*(14), 5419–5454. Retrieved 2023-03-29, from https://journals.ametsoc.org/doi/10.1175/JCLI-D-16-0758.1 doi: 10.1175/JCLI-D-16-0758.1

Gordon, N. D., & Klein, S. A. (2014, May). Low-cloud optical depth feedback in climate models: Optical Depth Feedback. *Journal of Geophysical Research: Atmospheres*, *119*(10), 6052–6065. Retrieved 2022-03-29, from http://doi.wiley.com/10.1002/2013JD021052 doi: 10.1002/2013JD021052

Held, I. M., & Soden, B. J. (2006, November). Robust Responses of the Hydrological Cycle to Global Warming. *Journal of Climate*, *19*(21), 5686–5699. Retrieved 2022-09-02, from http://journals.ametsoc.org/doi/10.1175/JCLI3990.1 doi: 10.1175/JCLI3990.1

Jeffery, C. A., & Austin, P. H. (1997, November). Homogeneous nucleation of supercooled water: Results from a new equation of state. *Journal of Geophysical Research: Atmospheres*, *102*(D21), 25269–25279. Retrieved 2023-03-21, from http://doi.wiley.com/10.1029/97JD02243 doi: 10.1029/97JD02243

Jiang, J. H., Su, H., Zhai, C., Perun, V. S., Del Genio, A., Nazarenko, L. S., ... Stephens, G. L. (2012, July). Evaluation of cloud and water vapor simulations in CMIP5 climate models using NASA "A-Train" satellite observations: EVALUATION OF IPCC AR5 MODEL SIMULATIONS. *Journal of Geophysical Research: Atmospheres*, *117*(D14), n/a–n/a. Retrieved 2023-02-03, from http://doi.wiley.com/10.1029/2011JD017237 doi: 10.1029/2011JD017237

Klein, S. A., Hall, A., Norris, J. R., & Pincus, R. (2017, November). Low-Cloud Feedbacks from Cloud-Controlling Factors: A Review. *Surveys in Geophysics*, *38*(6), 1307–1329. Retrieved 2021-06-21, from http://link.springer.com/10.1007/s10712-017-9433-3 doi: 10.1007/s10712-017-9433-3

Klein, S. A., & Hartmann, D. L. (1993, August). The Seasonal Cycle of Low Stratiform Clouds. *Journal of Climate*, *6*(8), 1587–1606. Retrieved 2023-03-12, from http://journals.ametsoc.org/doi/10.1175/1520-0442(1993)006<1587:TSCOLS>2.0.CO;2 doi: 10.1175/1520-0442(1993)006⟨1587:TSCOLS⟩2.0.CO;2

Komurcu, M., Storelvmo, T., Tan, I., Lohmann, U., Yun, Y., Penner, J. E., ... Takemura, T. (2014, March). Intercomparison of the cloud water phase among global climate models: CLOUD WATER PHASE IN GCMs. *Journal of Geophysical Research: Atmospheres*, *119*(6), 3372–3400. Retrieved 2023-03-23, from http://doi.wiley.com/10.1002/2013JD021119 doi: 10.1002/2013JD021119

Konsta, D., Dufresne, J., Chepfer, H., Vial, J., Koshiro, T., Kawai, H., ... Ogura, T. (2022, June). Low-Level Marine Tropical Clouds in Six CMIP6 Models Are Too Few, Too Bright but Also Too Compact and Too Homogeneous. *Geophysical Research Letters*, *49*(11). Retrieved 2023-03-30, from https://onlinelibrary.wiley.com/doi/10.1029/2021GL097593 doi:

10.1029/2021GL097593

Koop, T., Luo, B., Tsias, A., & Peter, T. (2000, August). Water activity as the determinant for homogeneous ice nucleation in aqueous solutions. *Nature*, *406*(6796), 611–614. Retrieved 2023-03-21, from http://www.nature.com/articles/35020537 doi: 10.1038/35020537

Lacis, A. A., & Hansen, J. (1974, January). A Parameterization for the Absorption of Solar Radiation in the Earth's Atmosphere. *Journal of the Atmospheric Sciences*, *31*(1), 118–133. Retrieved 2023-03-30, from http://journals.ametsoc.org/doi/10.1175/1520-0469(1974)031<0118:APFTAO>2.0.CO;2 doi: 10.1175/1520-0469(1974)031⟨0118:APFTAO⟩2.0.CO;2

Lamb, D., & Verlinde, J. (2011). *Physics and Chemistry of Clouds* (1st ed.). Cambridge University Press. Retrieved 2023-03-21, from https://www.cambridge.org/core/product/identifier/9780511976377/type/book doi: 10.1017/CBO9780511976377

Liou, K.-N. (2002). *An introduction to atmospheric radiation* (2nd ed ed.). Amsterdam: Academic Press. (OCLC: 156781712)

Loeb, N. G., Doelling, D. R., Wang, H., Su, W., Nguyen, C., Corbett, J. G., . . . Kato, S. (2018, January). Clouds and the Earth's Radiant Energy System (CERES) Energy Balanced and Filled (EBAF) Top-of-Atmosphere (TOA) Edition-4.0 Data Product. *Journal of Climate*, *31*(2), 895–918. Retrieved 2023-01-19, from https://journals.ametsoc.org/doi/10.1175/JCLI-D-17-0208.1 doi: 10.1175/JCLI-D-17-0208.1

Lorenz, D. J., & DeWeaver, E. T. (2007, July). The Response of the Extratropical Hydrological Cycle to Global Warming. *Journal of Climate*, *20*(14), 3470–3484. Retrieved 2023-04-19, from http://journals.ametsoc.org/doi/10.1175/JCLI4192.1 doi: 10.1175/JCLI4192.1

Lubin, D., Zhang, D., Silber, I., Scott, R. C., Kalogeras, P., Battaglia, A., . . . Vogelmann, A. M. (2020, July). AWARE: The Atmospheric Radiation Measurement (ARM) West Antarctic Radiation Experiment. *Bulletin of the American Meteorological Society*, *101*(7), E1069–E1091. Retrieved 2023-04-13, from https://journals.ametsoc.org/view/journals/bams/101/7/bamsD180278.xml doi: 10.1175/BAMS-D-18-0278.1

Manaster, A., O'Dell, C. W., & Elsaesser, G. (2017, August). Evaluation of Cloud Liquid Water Path Trends Using a Multidecadal Record of Passive Microwave Observations. *Journal of Climate*, *30*(15), 5871–5884. Retrieved 2023-01-24, from https://journals.ametsoc.org/doi/10.1175/JCLI-D-16-0399.1 doi: 10.1175/JCLI-D-16-0399.1

McCoy, D. T., Eastman, R., Hartmann, D. L., & Wood, R. (2017, May). The Change in Low Cloud Cover in a Warmed Climate Inferred from AIRS, MODIS, and ERA-Interim. *Journal of Climate*, *30*(10), 3609–3620. Retrieved 2022-03-27, from http://journals.ametsoc.org/doi/10.1175/JCLI-D-15-0734.1 doi: 10.1175/JCLI-D-15-0734.1

McCoy, D. T., Field, P., Bodas-Salcedo, A., Elsaesser, G. S., & Zelinka, M. D. (2020, December). A Regime-Oriented Approach to Observationally Constraining Extratropical Shortwave Cloud Feedbacks. *Journal of Climate*, *33*(23), 9967–9983. Retrieved 2020-11-29, from https://journals.ametsoc.org/jcli/article/33/23/9967/354498/A-Regime-Oriented-Approach-to-Observationally (Publisher: American Meteorological Society) doi: 10.1175/JCLI-D-19-0987.1

McCoy, D. T., Field, P., Frazer, M. E., Zelinka, M. D., Elsaesser, G. S., Mülmenstädt, J., . . . Lebo, Z. J. (2022, April). Extratropical Shortwave Cloud Feedbacks in the Context of the Global Circulation and Hydrological Cycle. *Geophysical Research Letters*, *49*(8). Retrieved 2022-09-13, from https://onlinelibrary.wiley.com/doi/10.1029/2021GL097154 doi: 10.1029/2021GL097154

McCoy, D. T., Field, P., Gordon, H., Elsaesser, G. S., & Grosvenor, D. P. (2020, April). Untangling causality in midlatitude aerosol–cloud adjustments. *Atmospheric Chemistry and Physics*, *20*(7), 4085–4103. Retrieved 2023-04-13, from https://acp.copernicus.org/articles/20/4085/2020/ doi: 10.5194/acp-20-4085-2020

McCoy, D. T., Field, P. R., Elsaesser, G. S., Bodas-Salcedo, A., Kahn, B. H., Zelinka, M. D., … Wilkinson, J. (2019, January). Cloud feedbacks in extratropical cyclones: insight from long-term satellite data and high-resolution global simulations. *Atmospheric Chemistry and Physics*, *19*(2), 1147–1172. Retrieved 2022-09-02, from https://acp.copernicus.org/articles/19/1147/2019/ doi: 10.5194/acp-19-1147-2019

McCoy, D. T., Field, P. R., Schmidt, A., Grosvenor, D. P., Bender, F. A.-M., Shipway, B. J., … Elsaesser, G. S. (2018, April). Aerosol midlatitude cyclone indirect effects in observations and high-resolution simulations. *Atmospheric Chemistry and Physics*, *18*(8), 5821–5846. Retrieved 2022-05-20, from https://acp.copernicus.org/articles/18/5821/2018/ doi: 10.5194/acp-18-5821-2018

McCoy, D. T., Hartmann, D. L., & Grosvenor, D. P. (2014a, December). Observed Southern Ocean Cloud Properties and Shortwave Reflection. Part I: Calculation of SW Flux from Observed Cloud Properties*. *Journal of Climate*, *27*(23), 8836–8857. Retrieved 2022-12-21, from http://journals.ametsoc.org/doi/10.1175/JCLI-D-14-00287.1 doi: 10.1175/JCLI-D-14-00287.1

McCoy, D. T., Hartmann, D. L., & Grosvenor, D. P. (2014b, December). Observed Southern Ocean Cloud Properties and Shortwave Reflection. Part II: Phase Changes and Low Cloud Feedback*. *Journal of Climate*, *27*(23), 8858–8868. Retrieved 2022-12-21, from http://journals.ametsoc.org/doi/10.1175/JCLI-D-14-00288.1 doi: 10.1175/JCLI-D-14-00288.1

McCoy, D. T., Tan, I., Hartmann, D. L., Zelinka, M. D., & Storelvmo, T. (2016, June). On the relationships among cloud cover, mixed-phase partitioning, and planetary albedo in GCMs. *Journal of Advances in Modeling Earth Systems*, *8*(2), 650–668. Retrieved 2022-06-14, from https://onlinelibrary.wiley.com/doi/10.1002/2015MS000589 doi: 10.1002/2015MS000589

Mossop, S. C. (1985, March). The Origin and Concentration of Ice Crystals in Clouds. *Bulletin of the American Meteorological Society*, *66*(3), 264–273. Retrieved 2023-03-21, from http://journals.ametsoc.org/doi/10.1175/1520-0477(1985)066<0264:TOACOI>2.0.CO;2 doi: 10.1175/1520-0477(1985)066⟨0264:TOACOI⟩2.0.CO;2

Myers, T. A., & Norris, J. R. (2013, October). Observational Evidence That Enhanced Subsidence Reduces Subtropical Marine Boundary Layer Cloudiness. *Journal of Climate*, *26*(19), 7507–7524. Retrieved 2021-12-06, from http://journals.ametsoc.org/doi/10.1175/JCLI-D-12-00736.1 doi: 10.1175/JCLI-D-12-00736.1

Myers, T. A., & Norris, J. R. (2015, April). On the Relationships between Subtropical Clouds and Meteorology in Observations and CMIP3 and CMIP5 Models*. *Journal of Climate*, *28*(8), 2945–2967. Retrieved 2023-04-13, from http://journals.ametsoc.org/doi/10.1175/JCLI-D-14-00475.1 doi: 10.1175/JCLI-D-14-00475.1

Myers, T. A., & Norris, J. R. (2016, March). Reducing the uncertainty in subtropical cloud feedback. *Geophysical Research Letters*, *43*(5), 2144–2148. Retrieved 2021-12-06, from https://onlinelibrary.wiley.com/doi/10.1002/2015GL067416 doi: 10.1002/2015GL067416

Myers, T. A., Scott, R. C., Zelinka, M. D., Klein, S. A., Norris, J. R., & Caldwell, P. M. (2021, June). Observational constraints on low cloud feedback reduce uncertainty of climate sensitivity. *Nature Climate Change*, *11*(6), 501–507. Retrieved 2021-06-21, from http://www.nature.com/articles/

s41558-021-01039-0 doi: 10.1038/s41558-021-01039-0

Nam, C., Bony, S., Dufresne, J.-L., & Chepfer, H. (2012, November). The 'too few, too bright' tropical low-cloud problem in CMIP5 models: TOO FEW TOO BRIGHT LOW-CLOUDS. *Geophysical Research Letters*, *39*(21), n/a–n/a. Retrieved 2023-03-30, from http://doi.wiley.com/10.1029/2012GL053421 doi: 10.1029/2012GL053421

O'Dell, C. W., Wentz, F. J., & Bennartz, R. (2008, April). Cloud Liquid Water Path from Satellite-Based Passive Microwave Observations: A New Climatology over the Global Oceans. *Journal of Climate*, *21*(8), 1721–1739. Retrieved 2023-02-02, from http://journals.ametsoc.org/doi/10.1175/2007JCLI1958.1 doi: 10.1175/2007JCLI1958.1

Paltridge, G. W. (1980, October). Cloud-radiation feedback to climate. *Quarterly Journal of the Royal Meteorological Society*, *106*(450), 895–899. Retrieved 2023-02-22, from https://onlinelibrary.wiley.com/doi/10.1002/qj.49710645018 doi: 10.1002/qj.49710645018

Qu, X., Hall, A., Klein, S. A., & DeAngelis, A. M. (2015, September). Positive tropical marine low-cloud cover feedback inferred from cloud-controlling factors. *Geophysical Research Letters*, *42*(18), 7767–7775. Retrieved 2021-03-28, from https://onlinelibrary.wiley.com/doi/10.1002/2015GL065627 doi: 10.1002/2015GL065627

Schaller, R. C., & Fukuta, N. (1979, September). Ice Nucleation by Aerosol Particles: Experimental Studies Using a Wedge-Shaped Ice Thermal Diffusion Chamber. *Journal of the Atmospheric Sciences*, *36*(9), 1788–1802. Retrieved 2023-03-21, from http://journals.ametsoc.org/doi/10.1175/1520-0469(1979)036<1788:INBAPE>2.0.CO;2 doi: 10.1175/1520-0469(1979)036⟨1788:INBAPE⟩2.0.CO;2

Schubert, W. H., Wakefield, J. S., Steiner, E. J., & Cox, S. K. (1979, July). Marine Stratocumulus Convection. part II: Horizontally Inhomogeneous Solutions. *Journal of the Atmospheric Sciences*, *36*(7), 1308–1324. Retrieved 2023-03-17, from http://journals.ametsoc.org/doi/10.1175/1520-0469(1979)036<1308:MSCPIH>2.0.CO;2 doi: 10.1175/1520-0469(1979)036⟨1308:MSCPIH⟩2.0.CO;2

Seager, R., & Henderson, N. (2013, October). Diagnostic Computation of Moisture Budgets in the ERA-Interim Reanalysis with Reference to Analysis of CMIP-Archived Atmospheric Model Data*. *Journal of Climate*, *26*(20), 7876–7901. Retrieved 2021-03-28, from http://journals.ametsoc.org/doi/10.1175/JCLI-D-13-00018.1 doi: 10.1175/JCLI-D-13-00018.1

Senior, C. A., & Mitchell, J. F. B. (1993, March). Carbon Dioxide and Climate. The Impact of Cloud Parameterization. *Journal of Climate*, *6*(3), 393–418. Retrieved 2023-02-22, from http://journals.ametsoc.org/doi/10.1175/1520-0442(1993)006<0393:CDACTI>2.0.CO;2 doi: 10.1175/1520-0442(1993)006⟨0393:CDACTI⟩2.0.CO;2

Sherwood, S. C., Bony, S., & Dufresne, J.-L. (2014, January). Spread in model climate sensitivity traced to atmospheric convective mixing. *Nature*, *505*(7481), 37–42. Retrieved 2023-02-22, from http://www.nature.com/articles/nature12829 doi: 10.1038/nature12829

Sherwood, S. C., Webb, M. J., Annan, J. D., Armour, K. C., Forster, P. M., Hargreaves, J. C., … Zelinka, M. D. (2020, December). An Assessment of Earth's Climate Sensitivity Using Multiple Lines of Evidence. *Reviews of Geophysics*, *58*(4). Retrieved 2022-02-14, from https://onlinelibrary.wiley.com/doi/10.1029/2019RG000678 doi: 10.1029/2019RG000678

Siler, N., Roe, G. H., & Armour, K. C. (2018, September). Insights into the Zonal-Mean Response of the Hydrologic Cycle to Global Warming from a Diffusive Energy Balance Model. *Journal of Climate*, *31*(18), 7481–7493. Retrieved 2023-03-07, from https://journals.ametsoc.org/view/journals/clim/31/

18/jcli-d-18-0081.1.xml doi: 10.1175/JCLI-D-18-0081.1
Stephens, G. L., & Ellis, T. D. (2008, December). Controls of Global-Mean Precipitation Increases in Global Warming GCM Experiments. *Journal of Climate*, *21*(23), 6141–6155. Retrieved 2023-03-16, from http://journals.ametsoc.org/doi/10.1175/2008JCLI2144.1 doi: 10.1175/2008JCLI2144.1
Stevens, B., & Brenguier, J.-L. (2009). *Cloud-controlling Factors.*
Storelvmo, T., & Tan, I. (2015, July). The Wegener-Bergeron-Findeisen process – Its discovery and vital importance for weather and climate. *Meteorologische Zeitschrift*, *24*(4), 455–461. Retrieved 2023-01-18, from http://www.schweizerbart.de/papers/metz/detail/24/84731/The_Wegener_Bergeron_Findeisen_process__Its_discov?af=crossref doi: 10.1127/metz/2015/0626
Storelvmo, T., Tan, I., & Korolev, A. V. (2015, December). Cloud Phase Changes Induced by CO2 Warming—a Powerful yet Poorly Constrained Cloud-Climate Feedback. *Current Climate Change Reports*, *1*(4), 288–296. Retrieved 2023-02-22, from http://link.springer.com/10.1007/s40641-015-0026-2 doi: 10.1007/s40641-015-0026-2
Tan, I., Oreopoulos, L., & Cho, N. (2019, April). The Role of Thermodynamic Phase Shifts in Cloud Optical Depth Variations With Temperature. *Geophysical Research Letters*, *46*(8), 4502–4511. Retrieved 2023-04-10, from https://onlinelibrary.wiley.com/doi/10.1029/2018GL081590 doi: 10.1029/2018GL081590
Tan, I., Storelvmo, T., & Zelinka, M. D. (2016, April). Observational constraints on mixed-phase clouds imply higher climate sensitivity. *Science*, *352*(6282), 224–227. Retrieved 2023-01-18, from https://www.science.org/doi/10.1126/science.aad5300 doi: 10.1126/science.aad5300
Terai, C. R., Zhang, Y., Klein, S. A., Zelinka, M. D., Chiu, J. C., & Min, Q. (2019, February). Mechanisms Behind the Extratropical Stratiform Low-Cloud Optical Depth Response to Temperature in ARM Site Observations. *Journal of Geophysical Research: Atmospheres*, *124*(4), 2127–2147. Retrieved 2022-05-23, from https://onlinelibrary.wiley.com/doi/10.1029/2018JD029359 doi: 10.1029/2018JD029359
Trenberth, K. (2011, March). Changes in precipitation with climate change. *Climate Research*, *47*(1), 123–138. Retrieved 2023-03-16, from http://www.int-res.com/abstracts/cr/v47/n1-2/p123-138/ doi: 10.3354/cr00953
Trenberth, K. E. (1998, August). Atmospheric Moisture Residence Times and Cycling: Implications for Rainfall Rates and Climate Change. *Climatic Change*, *39*, 667–694. doi: 10.1023/A:1005319109110
Tukey, J. W. (1958, June). Bias and Confidence in Not-quite Large Samples. (Abstracts of Papers). *The Annals of Mathematical Statistics*, *29*(2), 614. Retrieved 2023-04-06, from http://projecteuclid.org/euclid.aoms/1177706647 doi: 10.1214/aoms/1177706647
Wall, C. J., Norris, J. R., Possner, A., McCoy, D. T., McCoy, I. L., & Lutsko, N. J. (2022, November). Assessing effective radiative forcing from aerosol–cloud interactions over the global ocean. *Proceedings of the National Academy of Sciences*, *119*(46), e2210481119. Retrieved 2023-01-26, from https://pnas.org/doi/10.1073/pnas.2210481119 doi: 10.1073/pnas.2210481119
Webb, M. J., Lock, A. P., Bretherton, C. S., Bony, S., Cole, J. N. S., Idelkadi, A., ... Zhao, M. (2015, November). The impact of parametrized convection on cloud feedback. *Philosophical Transactions of the Royal Society A: Mathematical, Physical and Engineering Sciences*, *373*(2054), 20140414. Retrieved 2023-02-22, from https://royalsocietypublishing.org/doi/10.1098/rsta.2014.0414 doi: 10.1098/rsta.2014.0414
Wielicki, B. A., Barkstrom, B. R., Harrison, E. F., Lee, R. B., Louis Smith, G., & Cooper, J. E. (1996, May). Clouds and the Earth's Radiant Energy Sys-

tem (CERES): An Earth Observing System Experiment. *Bulletin of the American Meteorological Society*, *77*(5), 853–868. Retrieved 2023-01-19, from http://journals.ametsoc.org/doi/10.1175/1520-0477(1996)077<0853:CATERE>2.0.CO;2 doi: 10.1175/1520-0477(1996)077⟨0853:CATERE⟩2.0.CO;2

Zelinka, M. D., Grise, K. M., Klein, S. A., Zhou, C., DeAngelis, A. M., & Christensen, M. W. (2018, October). Drivers of the Low-Cloud Response to Poleward Jet Shifts in the North Pacific in Observations and Models. *Journal of Climate*, *31*(19), 7925–7947. Retrieved 2023-04-13, from https://journals.ametsoc.org/doi/10.1175/JCLI-D-18-0114.1 doi: 10.1175/JCLI-D-18-0114.1

Zelinka, M. D., Klein, S. A., & Hartmann, D. L. (2012, June). Computing and Partitioning Cloud Feedbacks Using Cloud Property Histograms. Part II: Attribution to Changes in Cloud Amount, Altitude, and Optical Depth. *Journal of Climate*, *25*(11), 3736–3754. Retrieved 2022-05-26, from https://journals.ametsoc.org/doi/10.1175/JCLI-D-11-00249.1 doi: 10.1175/JCLI-D-11-00249.1

Zelinka, M. D., Myers, T. A., McCoy, D. T., Po-Chedley, S., Caldwell, P. M., Ceppi, P., … Taylor, K. E. (2020, January). Causes of Higher Climate Sensitivity in CMIP6 Models. *Geophysical Research Letters*, *47*(1). Retrieved 2021-11-29, from https://onlinelibrary.wiley.com/doi/abs/10.1029/2019GL085782 doi: 10.1029/2019GL085782

Zhai, C., Jiang, J. H., & Su, H. (2015, October). Long-term cloud change imprinted in seasonal cloud variation: More evidence of high climate sensitivity: Cloud Feedback and Seasonal Variation. *Geophysical Research Letters*, *42*(20), 8729–8737. Retrieved 2022-03-27, from http://doi.wiley.com/10.1002/2015GL065911 doi: 10.1002/2015GL065911

Zhao, M. (2014, March). An Investigation of the Connections among Convection, Clouds, and Climate Sensitivity in a Global Climate Model. *Journal of Climate*, *27*(5), 1845–1862. Retrieved 2023-02-22, from http://journals.ametsoc.org/doi/10.1175/JCLI-D-13-00145.1 doi: 10.1175/JCLI-D-13-00145.1

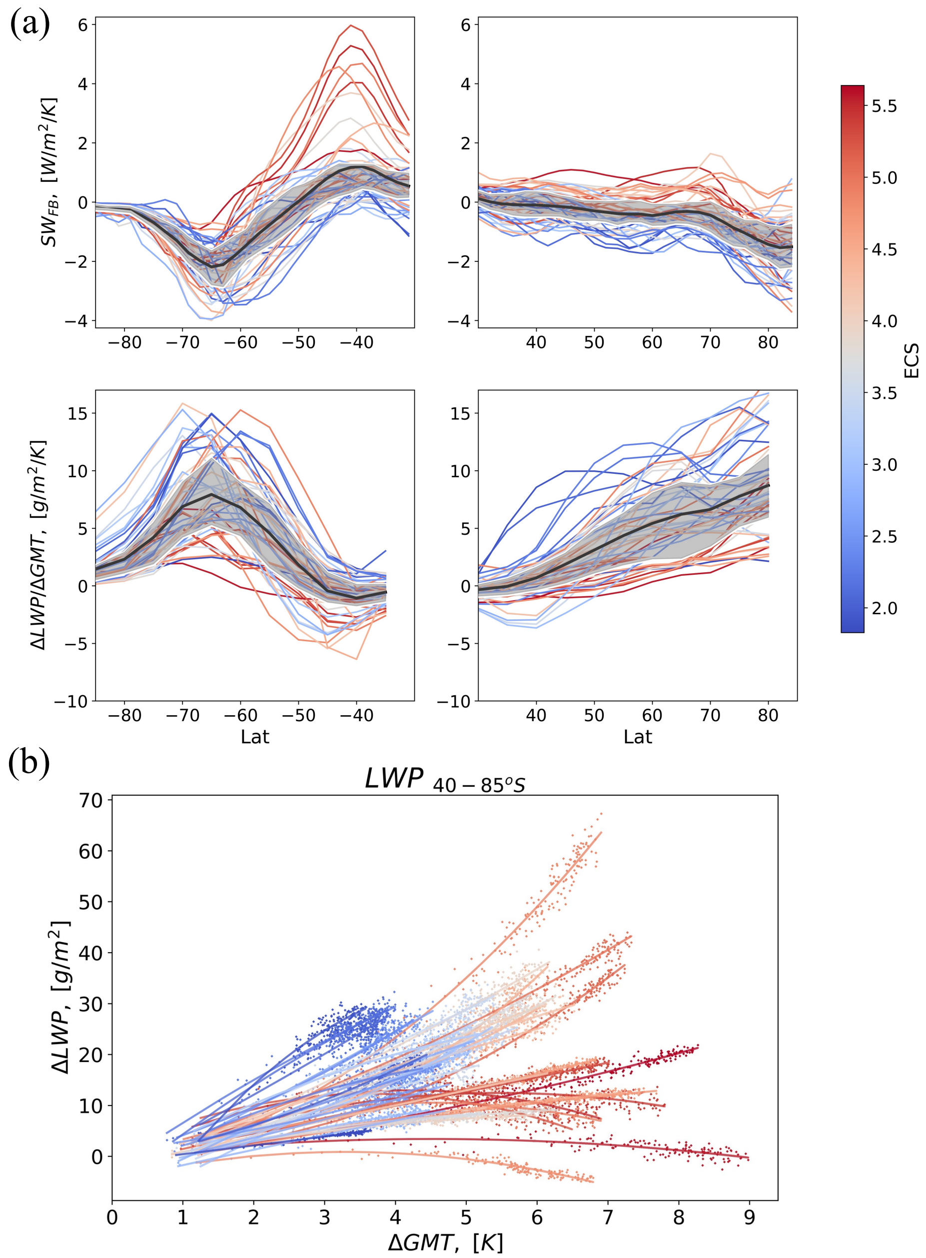

Figure 1. (a) Extratropical SW_{FB} (top) and the response of LWP to global-mean surface air temperature (GMT) ($\Delta LWP/\Delta GMT$) calculated as the difference *piControl* and years 121 - 140 from the $abrupt4xCO_2$ simulation. (b) Annual-mean anomalies in LWP relative to *piControl* averaged over $40 - 85^oS$ versus anomalies in GMT in the first 150 years of $abrupt4xCO_2$ simulations. The thick black lines in subplot (a) are the multi-model mean, and the shaded regions correspond to the 25th-75th percentiles of quantities. Lines in subplot (b) are the second-order polynomial fits of the annual LWP responses. SW cloud feedback and effective climate sensitivity (ECS) data are derived from Zelinka et al. (2020). Fifty CMIP5 and CMIP6 GCMs are shown (Table S1). Lines for each GCM in (a) and (b) are colored by the ECS for that specific GCM.

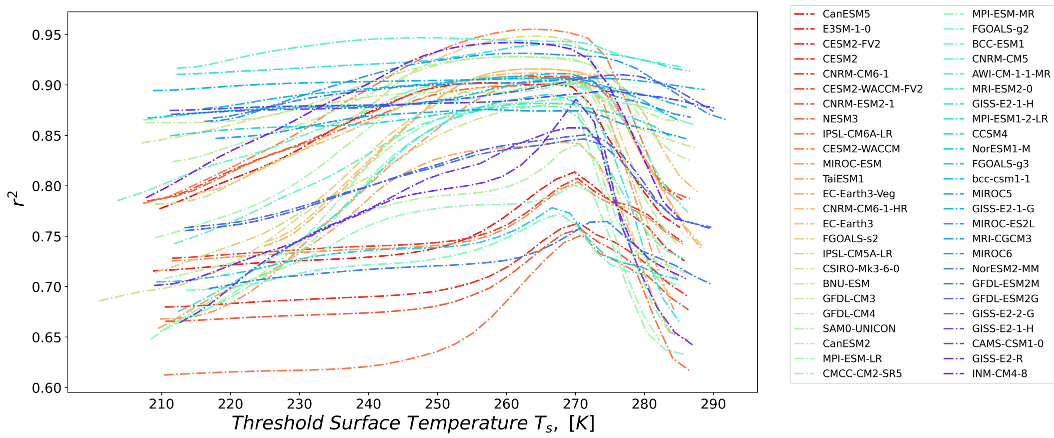

Figure 2. The r^2 between the LWP predicted by Equation 3 and GCM output in *piControl* simulations as a function of potential threshold surface temperature (TR_{T_s}) used to partition the cold and warm regimes in Equation 3. TR_{T_s} is selected to maximize r^2.

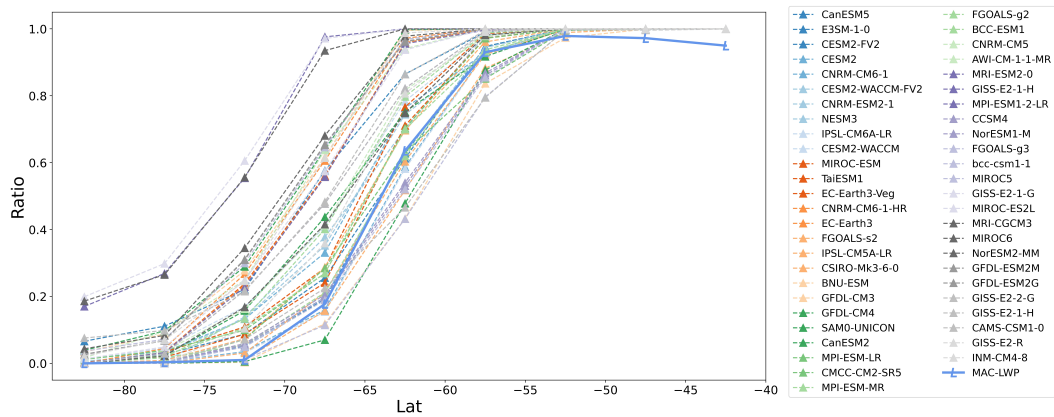

Figure 3. Latitudinal distribution of the ratio of gridboxes that are classified as warm regime to the total number of gridboxes for GCMs (dashed lines) and the ratio of gridboxes with more than 50% coverage in microwave retrievals to the total number of gridboxes for MAC-LWP observations (solid line).

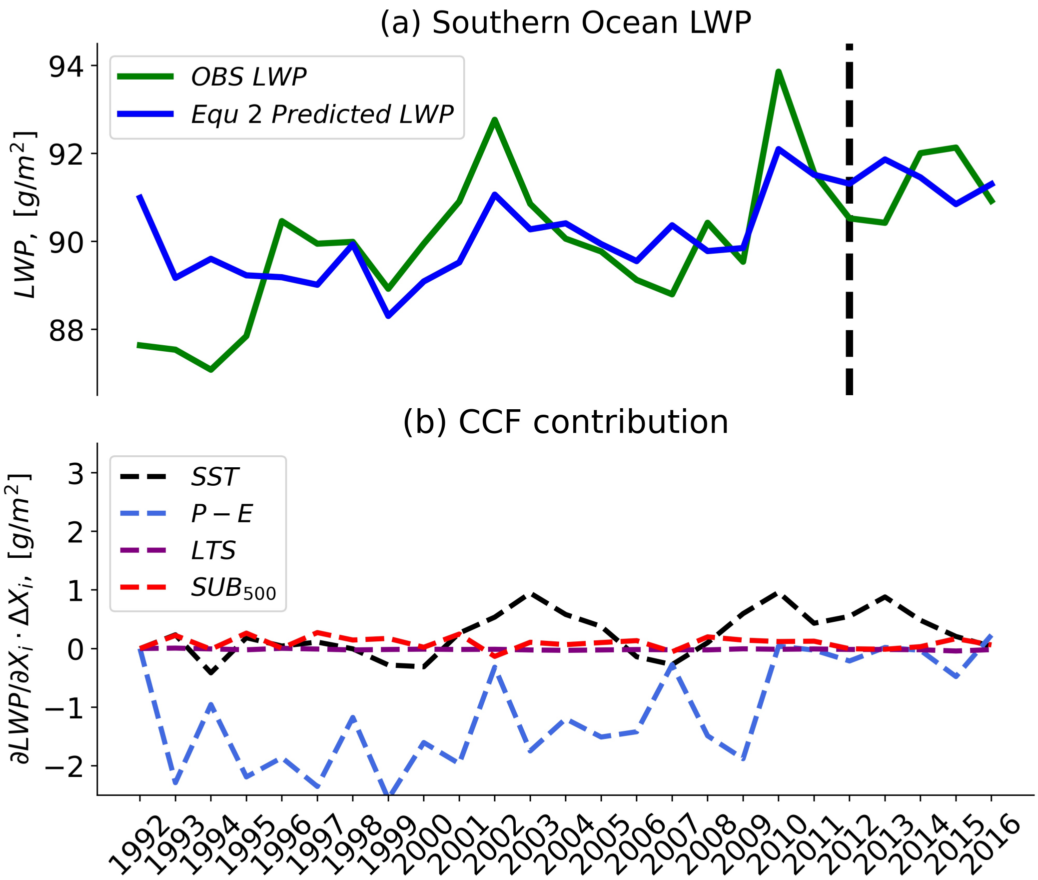

Figure 4. (a) Observed Southern Ocean annual-mean LWP from MAC-LWP (green) and LWP predicted by the CCF model (Equation 2; blue) from 1992 to 2016. The CCF model is trained on data from 2012 to 2016 (right side of the dashed line) and is used to predict LWP back to 1992. (b) The decomposition of annual mean LWP anomalies into individual CCF contributions by Equation 2.

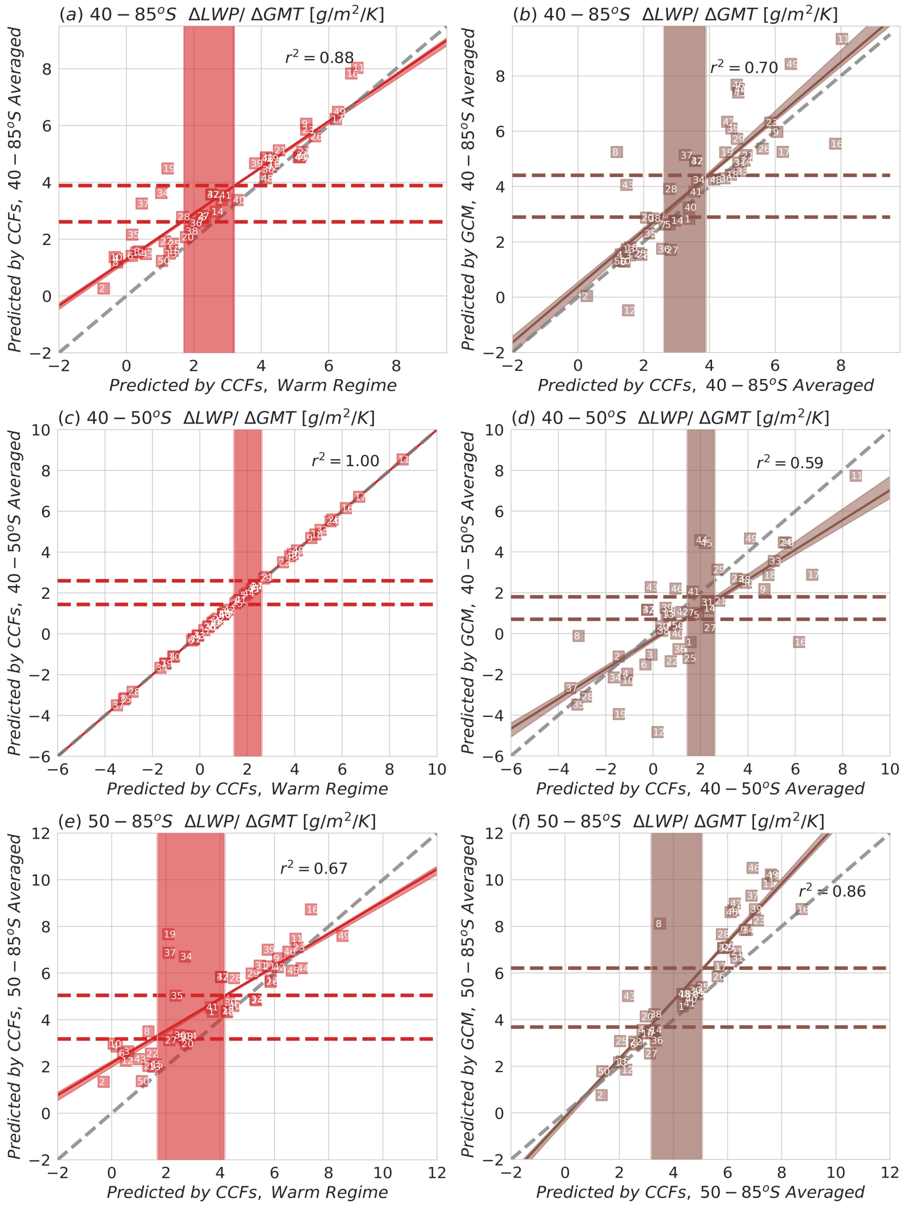

Figure 5. Predictions of the GCM-simulated $\Delta LWP/\Delta GMT$ by (Equation 3). $\Delta LWP/\Delta GMT$ is shown averaged over (a,b) $40-85^oS$, (c,d) $40-50^oS$, and (e,f): $50-85^oS$. (a,c,e) Predicted $\Delta LWP/\Delta GMT$ from Equation 3 versus $\Delta LWP/\Delta GMT$ in only the warm regime. (b,d,f) $\Delta LWP/\Delta GMT$ simulated by GCMs versus $\Delta LWP/\Delta GMT$ predicted by Equation 3 for all regimes. 1-1 lines are shown using dashed gray lines and best fit are shown as solid red and brown lines with their uncertainties estimated by Jackknife resampling. Observational constraints (red shading) are shown in (a,c,e). This constraint is propagated from the warm regime $\Delta LWP/\Delta GMT$ to the latitudinal-averaged $\Delta LWP/\Delta GMT$ by taking the intersection between the red shading and the fit line with its uncertainty (red dashed lines). Constraints on latitudinal-averaged $\Delta LWP/\Delta GMT$ are then shown using brown shading in (b,d,f). This is combined with the uncertainty in the CCF model prediction by using the best fit line between GCM and CCF model predictions to yield an observational constraint on GCM-simulated $\Delta LWP/\Delta GMT$. Explained variance (r^2) are shown within each subplot. GCMs are denoted with the number listed in Table S1.

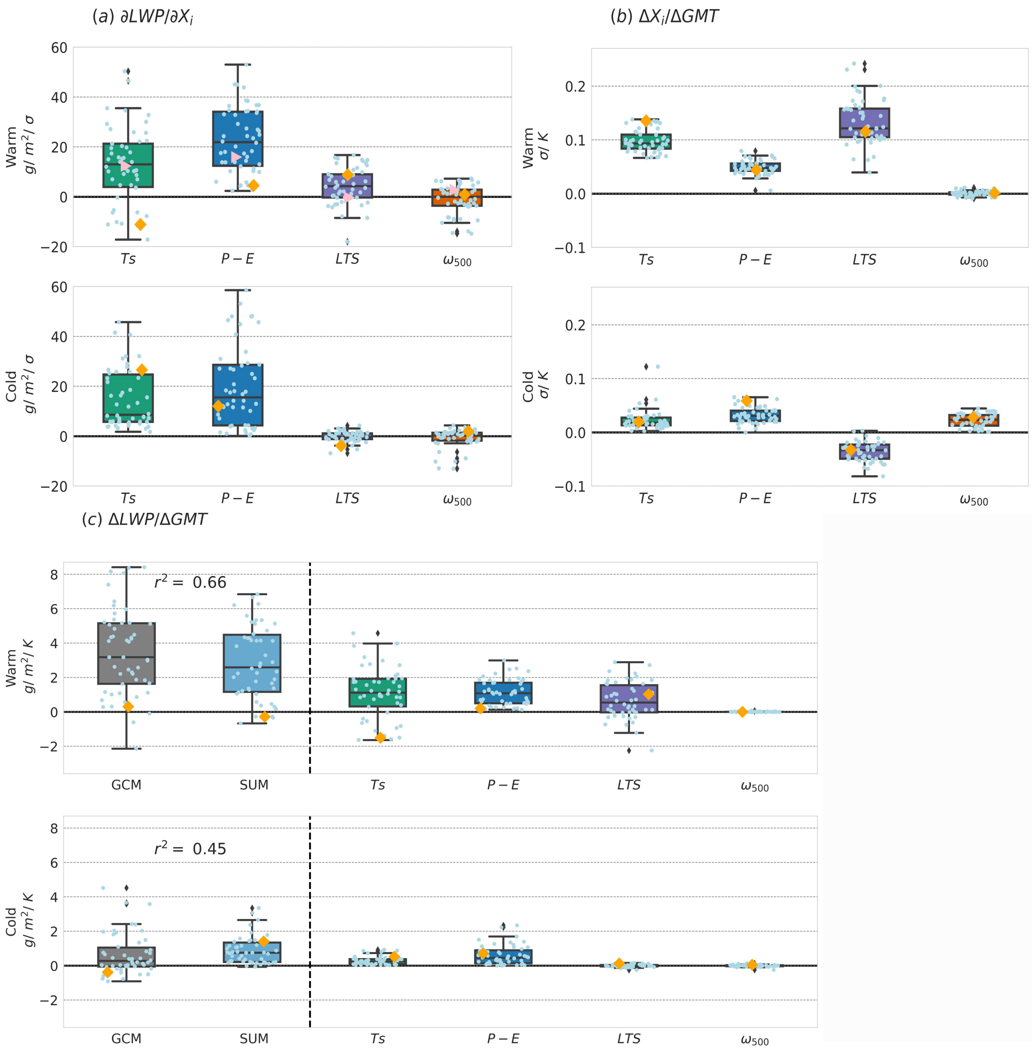

Figure 6. The contribution of each term in Equation 3 for $40 - 85^oS$ averaged LWP response to GMT for warm and cold regimes: (a) Sensitivities of LWP to CCFs in GCMs (observational sensitivities are shown as pink triangle markers in the warm regime); (b) Changes in each CCF per degree GMT change; (c) LWP changes due to individual CCFs (the product of (a) with (b)), their sum (light blue box), and the GCM response (gray box). The r^2 between Equation 3 predicted LWP response to GMT and the GCM output in each regime is noted. CCFs are normalized by their spatio-temporal standard deviations of each regime in the mean-state climate. CESM2 values are denoted by orange diamonds, all other GCMs are denoted by light blue dots.

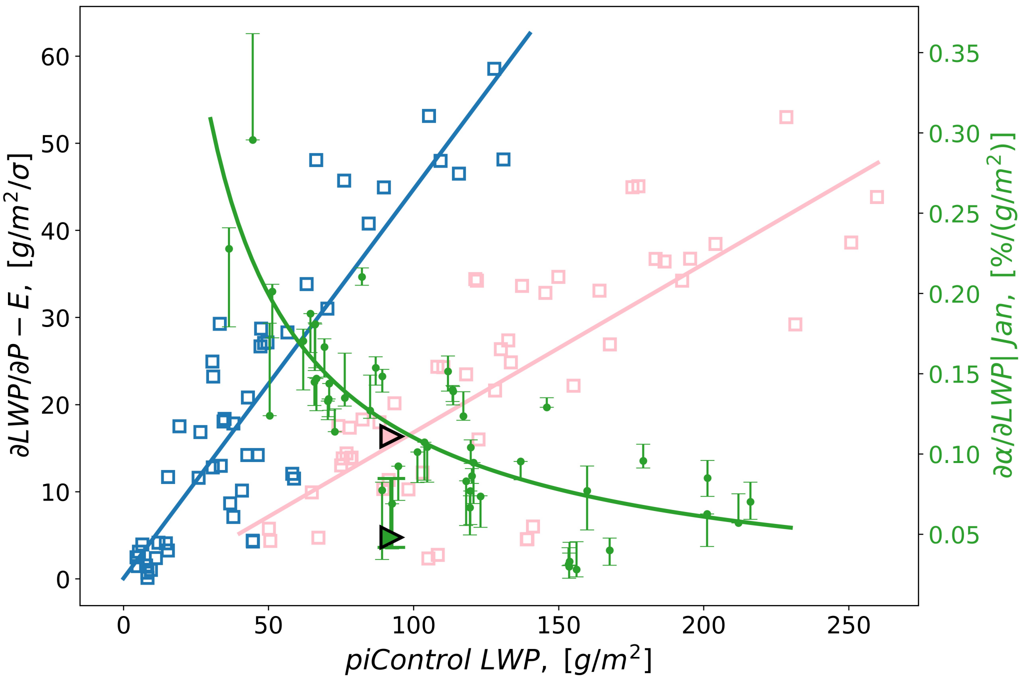

Figure 7. The sensitivity of LWP to moisture convergence ($\partial LWP/\partial P - E$, left axis) in the warm (red) and cold (blue) regimes and the radiative susceptibility ($\partial\alpha/\partial LWP$, right axis) as a function of mean-state (*piControl*) LWP. Observational $\partial LWP/\partial P - E$ and $\partial\alpha/\partial LWP$ are shown by the pink and green triangles (observational $\partial LWP/\partial P - E$ is comparable to the warm regime $\partial LWP/\partial P - E$ of GCMs for reason discussed in section 2.2 and 2.5). The linear fit between $\partial LWP/\partial P - E$ in each regime and *piControl* LWP and the power law fit between $\partial\alpha/\partial LWP$ and *piControl* LWP are shown. $\partial\alpha/\partial LWP$ for $TR_{\alpha_{cs}}$ be 0.15 is shown with marker and uncertainty from varying $TR_{\alpha_{cs}}$ from 0.11 to 0.30 is shown as the error bar.

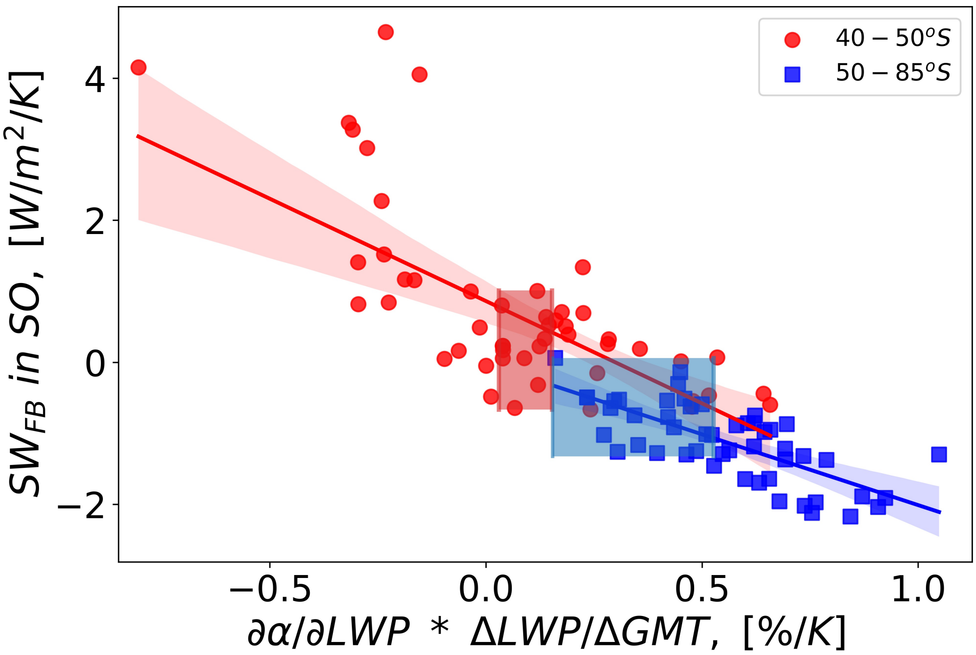

Figure 8. GCM SW cloud feedback (SW_{FB}) from Zelinka et al. (2020) as a function of SW_{FB} predicted by Equation 1 for $40-50^oS$ (red) and $50-85^oS$ (blue) latitude bands. Observational constraints on $40-50^oS$ and $50-85^oS$ $\Delta LWP/\Delta GMT$ are from Figure 5 (d) and (f) and the observational constrain on $\partial\alpha/\partial LWP$ is shown in Figure 7. The combination of these constraints yields constraints on $40-50^oS$ and $50-85^oS$ SW_{FB} shown as shaded regions along the x-axis. The linear fit between SW_{FB} and prediction from Equation 1 are shown with their 95% confidence interval. Constraints on $40-50^oS$ and $50-85^oS$ SW_{FB} are the extents of the y-coordinate of models within the shaded regions.

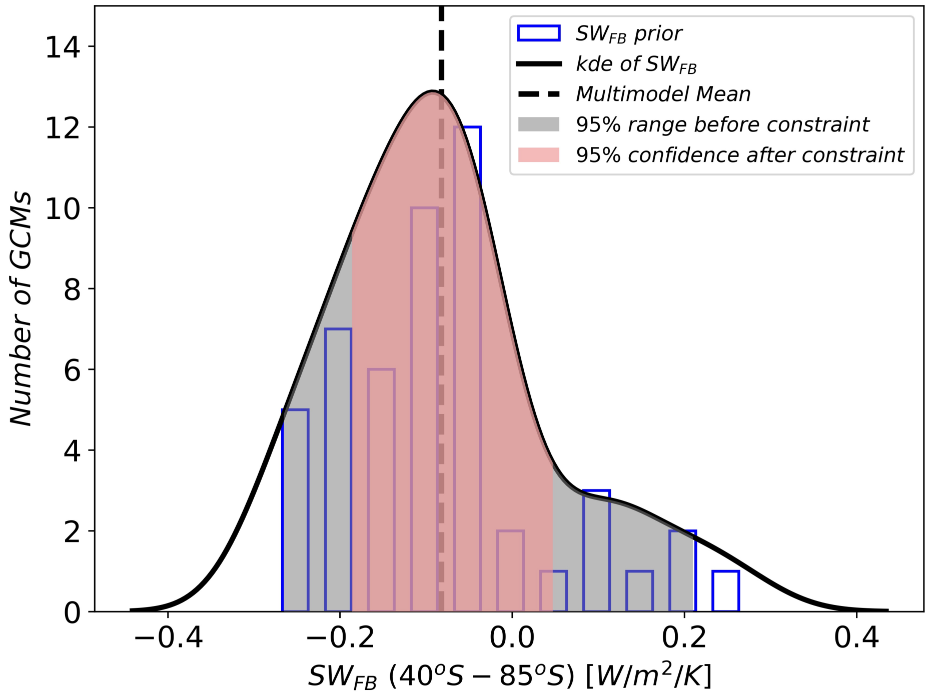

Figure 9. The contribution of Southern Ocean $(40 - 85^oS)$ SW_{FB} to the global mean cloud feedback. SW_{FB} for 50 CMIP5 and CMIP6 GCMs listed in Table S1 is shown as a blue histogram black kernel density estimate. A dashed black line denotes the multimodel mean SW_{FB}. Gray shading shows the 95% range of the model SW_{FB} before constraint. Red shading shows the 95% confidence interval of the Southern Ocean SW_{FB} by combining the $40 - 50^oS$ and $50 - 85^oS$ SW_{FB} constraints (Figure 8). Observational constraint suggests a moderate negative to weak positive Southern Ocean SW_{FB}.